

Unified description of the neutron-²⁰⁸Pb mean field between -20 and $+165$ MeV from the dispersion relation constraint

C. H. Johnson and D. J. Horen

Oak Ridge National Laboratory, Oak Ridge, Tennessee 37831

C. Mahaux

Institut de Physique B5, Université de Liège, B-4000 Liège 1, Belgium

(Received 11 June 1987)

The real part of the central neutron-²⁰⁸Pb mean field is the sum of a Hartree-Fock component plus a dispersive component. In keeping with theoretical expectations, the Hartree-Fock field is assumed to have a Woods-Saxon shape whose depth decreases exponentially with increasing energy and whose radius and diffuseness are independent of energy. The dispersive component is determined from the imaginary part of the optical-model potential by making use of the dispersion relation which connects these two quantities. The imaginary part is written as the sum of a volume and a surface-peaked contribution. The dispersion relation then implies that the real dispersive contribution is also the sum of volume and surface-peaked components. The parameters of the complex mean field are determined by fitting the available differential and polarization cross sections in the energy domain [4, 40 MeV] and the total cross sections in the domain [1, 120 MeV]; these data are contained in previous published or unpublished reports, but new measurements of the total cross sections are presented from 1 to 25 MeV. Good fits to these cross sections, and also to unpublished total cross sections for energies up to 165 MeV, are obtained despite the fact that the number of adjusted parameters is quite small because of our use of the constraint implied by the dispersion relation. The real part of the mean field is well approximated by a Woods-Saxon shape whose radius decreases with increasing energy between 5 and 25 MeV; its depth is approximately constant from 5 to 15 MeV and then decreases with increasing energy; these findings are in keeping with recent empirical evidence. When the neutron energy decreases below 2.5 MeV, the potential radius decreases; it increases again when the neutron energy decreases below -14.5 MeV. In the domain $-20 \text{ MeV} < E < 0$ the deduced potential accurately reproduces the experimental single-particle energies as well as the asymptotic values of the single-particle wave functions as measured from sub-Coulomb pickup reactions; it also yields excellent agreement with the spreading width of the deeply bound $1h_{11/2}$ hole state. The rms radii, absolute spectroscopic factors, and occupation numbers are calculated for the valence particle and hole states. At the Fermi energy (-6 MeV), the mean field can be identified with the Hartree-Fock potential, for which the present analysis yields a depth of 46.4 MeV, a radius of $1.24 A^{1/3}$ fm, and a diffuseness of 0.68 fm. In the energy domain $4 \leq E \leq 10$ MeV, the already good agreement between the predicted and measured cross sections is further improved if the imaginary part of the mean field is allowed to have its strength depend upon the neutron orbital angular momentum, and its surface diffuseness is allowed to be energy dependent.

I. INTRODUCTION

For bombarding energies E larger than a few MeV, accurate fits to the experimental nucleon elastic scattering cross sections can be obtained from an optical-model potential whose central part is local, viz.,

$$\mathcal{M}(r; E) = \mathcal{V}(r; E) + i\mathcal{W}(r; E). \quad (1.1)$$

Although the experimental data (differential, polarization, and total cross sections) at a given energy E can be quite detailed, they are not sufficient to enable one to carry out an accurate determination of the radial dependence of $\mathcal{V}(r; E)$ and $\mathcal{W}(r; E)$ from purely phenomenological analyses.¹ Accordingly, these analyses assume *a priori* some radial dependence for $\mathcal{V}(r; E)$ and $\mathcal{W}(r; E)$. They often adopt a Woods-Saxon shape for $\mathcal{V}(r; E)$, namely

$$\mathcal{V}(r; E) = V_v(E) f(X_v), \quad (1.2)$$

where

$$f(X_v) = [1 + \exp(X_v)]^{-1}, \quad (1.3a)$$

$$X_v = (r - R_v)/a_v, \quad (1.3b)$$

$$R_v = r_v A^{1/3}. \quad (1.3c)$$

Good fits to the experimental data at various energies are usually obtained by simply allowing the potential depth V_v to vary linearly with energy, while r_v and a_v are kept constant. However, recent accurate measurements and phenomenological analyses²⁻⁴ of the scattering of neutrons by ²⁰⁸Pb for energies between 4 and 40 MeV suggest the following empirical trends. (i) The well depth V_v is almost independent of energy between 4 and about 20 MeV, while for larger energy $|V_v|$ decreases

with increasing E . (ii) The potential radius R_V decreases with increasing energy between 4 and about 20 MeV, and remains approximately constant for larger energies. These features are compatible with the usual property that the volume integral per nucleon decreases with increasing scattering energy for E greater than a few MeV.

In the present paper we show that the empirical trends (i) and (ii) are in qualitative agreement with theoretical predictions based on the following dispersion relation (DR), which connects the real and the imaginary parts of the optical-model potential:⁵

$$\mathcal{V}(r;E) = \mathcal{V}_H(r;E) + \Delta\mathcal{V}(r;E), \quad (1.4)$$

$$\Delta\mathcal{V}(r;E) = \frac{P}{\pi} \int_{-\infty}^{\infty} \frac{\mathcal{W}(r;E')}{E' - E} dE'. \quad (1.5)$$

Here, P denotes a principal value integral and $\mathcal{V}_H(r;E)$ the Hartree-Fock contribution to the mean field. The quantity $\Delta\mathcal{V}(r;E)$ is the dispersive contribution to $\mathcal{V}(r;E)$; essentially, it is the correction to $\mathcal{V}_H(r;E)$ which is due to the fact that the target does not remain in its ground state during the elastic scattering process.

The energy dependence of $\mathcal{V}_H(r;E)$ is expected to be quite smooth (Sec. IIB). This is not the case for $\Delta\mathcal{V}(r;E)$. Indeed, the DR, Eq. (1.5), has two main implications: (i) $\Delta\mathcal{V}(r;E)$ has a distinct energy dependence for small $|E|$ since $|\mathcal{W}(r;E')|$ rapidly decreases with decreasing E' because of threshold effects. (ii) $\Delta\mathcal{V}(r;E)$ is the sum of a volume contribution (Woods-Saxon shape) and of a surface-peaked component (derivative of a Woods-Saxon shape), since $\mathcal{W}(r;E)$ is empirically found to be described by that radial structure. Therefore, the dispersive contribution $\Delta\mathcal{V}(r;E)$ gives rise not only to an energy dependence of the central depth of $\mathcal{V}(r;E)$, but also to an energy dependence in the radial shape (since a surface-peaked contribution, in effect, changes the radius of the Woods-Saxon potential to which it is added⁶). We shall see that this energy dependence is not simple at small energies, in contrast to that of $\mathcal{V}_H(r;E)$. Accordingly, it appears appropriate to take the constraint (1.5) explicitly into account in optical-model analyses.

The DR constraint proves particularly crucial when one extrapolates the optical-model potential toward negative energies, i.e., if one wants to study the smooth but nontrivial transition between the optical-model potential and the shell-model potential. Here we use the traditional terminology in which $\mathcal{M}(r;E)$ is called “the optical-model potential” for $E > 0$ (scattering states) and “the shell-model potential” for $E < 0$ (bound states). We emphasize, however, that $\mathcal{M}(r;E)$ is a continuous function of E . One of our primary purposes is to extrapolate $\mathcal{M}(r;E)$ from positive E , where many experimental data are available, towards negative E , where the experimental information is much more scarce.

Our main aim is therefore twofold. Firstly, we implement the DR constraint, Eq. (1.5), in the optical-model analysis of the experimental scattering data for neutrons on ²⁰⁸Pb. Secondly, we extrapolate the constructed potential $\mathcal{V}(r;E)$ towards negative energies; there we compare the eigenvalues associated with $\mathcal{V}(r;E)$ to the ex-

perimental energies of weakly and deeply bound single-particle valence and hole states. We also compare the single-particle wave functions at large distance with the experimental values obtained from the analysis of sub-Coulomb pickup reactions.

Our presentation will be the following. A simple “fixed-geometry” model is described in Sec. II, where we specify our assumptions and procedure. This simple model contains only a few unknown constants. These unknowns are determined in Sec. III from the analysis of a quite complete set of experimental cross sections (differential and polarization cross sections between 4 and 40 MeV, and total cross sections between 1 and 120 MeV). Most of these data have been published previously, but we shall also present previously unpublished total cross sections. We show that the model yields very good agreement with these experimental data, despite the fact that only a few adjustable parameters are available, because of our use of the DR. Section IV deals with the extrapolation of the potential $\mathcal{V}(r;E)$ towards negative energies, where it should be identified with the shell-model potential. We demonstrate that our extrapolation, which is analytic and involves no additional parameter, yields very good agreement with the experimental energies of the weakly and deeply bound single-particle states and the spreading width of the deeply bound $1h_{11/2}$ hole state. We also show that the predicted single-particle wave functions at large distance are in excellent agreement with the experimental values deduced from sub-Coulomb pickup experiments. The “absolute” spectroscopic factors and occupation numbers are also computed. The energy dependence of the radial shape of $\mathcal{V}(r;E)$ is discussed in Sec. V. We show that the model accounts for the main empirical findings of Refs. 2–4, namely (i) Woods-Saxon shape with approximately constant depth but decreasing radius when E increases from 4 to about 20 MeV and, (ii) Woods-Saxon shape with decreasing depth and nearly constant radius for $20 < E < 40$ MeV. For $-14.5 < E < 2.5$ MeV, we find that the potential radius decreases with decreasing energy. Two possible refinements are considered in Secs. VI and VII. In Sec. VI we allow the geometry parameters of the surface absorptive potential to vary with energy for $E \leq 10$ MeV. In Sec. VII we consider a model in which $\mathcal{W}(r;E)$ depends on the neutron orbital angular momentum; via the DR this also gives rise to an angular-momentum dependence for the real part $\mathcal{V}(r;E)$. This refined model not only improves the agreement with the experimental cross section in the low energy domain $4 \leq E \leq 11$ MeV, but also yields a better description of the empirical $\mathcal{V}(r;E)$ in the framework of the DR approach. Finally, Sec. VIII contains our conclusions.

II. MEAN FIELD MODEL WITH DR CONSTRAINT

A. Spin-orbit coupling

In addition to its central component, Eq. (1.1), the mean field contains a spin-orbit component for which we take the standard form

$$\mathcal{V}_{\text{so}}(r;E) = (\boldsymbol{\sigma} \cdot \mathbf{l})(\hbar/m_{\pi}c)^2 V_{\text{so}} \left[\frac{1}{r} \right] \frac{d}{dr} f(X_{\text{so}}), \quad (2.1)$$

where $f(X_{\text{so}})$ is the Woods-Saxon form factor defined by Eqs. (1.3a)–(1.3c). Throughout the present paper, we adopt the same spin-orbit parameters as in Ref. 4, namely

$$V_{\text{so}} = 5.75 \text{ MeV}, \quad r_{\text{so}} = 1.105 \text{ fm}, \quad a_{\text{so}} = 0.50 \text{ fm}. \quad (2.2)$$

We therefore no longer explicitly refer to this spin-orbit coupling; accordingly, we make no distinction between the full mean field and its central component $\mathcal{M}(r;E)$, Eq. (1.1).

B. Hartree-Fock contribution

The Hartree-Fock (HF) contribution can be interpreted as the mean field that would be obtained if one would make the approximation that the target remains in its ground state throughout the scattering process and, furthermore, that this ground state is described by the independent particle model, i.e., that no nucleon-nucleon correlations exist in the target. This interpretation is natural in view of Eqs. (1.4) and (1.5): $\mathcal{V}_H(r;E)$ is the mean field obtained in the approximation where $\mathcal{W}(r;E)$ is set equal to zero, i.e., where collisions are neglected.

The HF contribution $\mathcal{V}_H(r;E)$ is the local equivalent of a nonlocal energy independent operator $\bar{\mathcal{V}}_H(\mathbf{r},\mathbf{r}')$: the energy dependence of $\mathcal{V}_H(r;E)$ is due to the replacement of a nonlocal potential by a local one. The available Hartree-Fock calculations indicate that, in a heavy nucleus such as ^{208}Pb , $\mathcal{V}_H(r;E)$ can be approximated by a Woods-Saxon potential:

$$\mathcal{V}_H(r;E) = V_H(E)f(X_H). \quad (2.3)$$

In the case of Skyrme-type effective nucleon-nucleon interactions, the geometric parameters r_H and a_H are practically independent of energy.⁷ Likewise, the Brueckner-Hartree-Fock approximation to the real part of the optical model yields a radial shape which is practically independent of energy.^{8,9} We shall accordingly make the assumption that the HF geometrical parameters r_H and a_H are independent of energy.

The Hartree-Fock potential associated with a Skyrme-type effective nucleon-nucleon interaction leads to a linear energy dependence of $V_H(E)$. This is a specific feature of the type of momentum dependence of the Skyrme interaction. It is not realistic when a wide range of energies is considered.⁷ A more realistic parametrization was postulated by Perey and Buck¹⁰ in their pioneering work, in which the nonlocality of $\bar{\mathcal{V}}_H(\mathbf{r},\mathbf{r}')$ has a Gaussian form:

$$\bar{\mathcal{V}}_H(\mathbf{r},\mathbf{r}') = \mathcal{V}(r)\exp(-|\mathbf{r}-\mathbf{r}'|^2/\beta^2), \quad (2.4)$$

where β is the range of nonlocality. The local energy approximation then yields¹⁰

$$V_H(E) = V_H(0)\exp[-\alpha V_H(0)]\exp\{-\alpha[E - V_H(E)]\}, \quad (2.5)$$

where

$$\alpha = (m/2\hbar^2)\beta^2. \quad (2.6)$$

Equation (2.5) suggests that $V_H(E)$ can be approximated by an exponential function of E :

$$V_H(E) = V_H(0)\exp(-\alpha E). \quad (2.7)$$

This approximation is expected to be realistic for $E < 150$ MeV; it would become unrealistic at high energy ($E > 200$ MeV) where $V_H(E)$ is empirically known to change sign. The dashed curve in Fig. 1(a) illustrates an exponential dependence for $V_H(E)$ for the 150-MeV energy domain above the Fermi energy E_F .

C. Imaginary part of the mean field

Phenomenological optical-model analyses indicate that the imaginary part $\mathcal{W}(r;E)$ of the optical-model potential can be represented by the sum of “volume” and “surface” contributions, viz.,

$$\mathcal{W}(r;E) = \mathcal{W}_v(r;E) + \mathcal{W}_s(r;E). \quad (2.8)$$

We shall make the usual assumption that the volume component has a Woods-Saxon shape and that the surface contribution is proportional to the radial derivative of a Woods-Saxon form factor:

$$\mathcal{W}_v(r;E) = W_v(E)f(X_W), \quad (2.9)$$

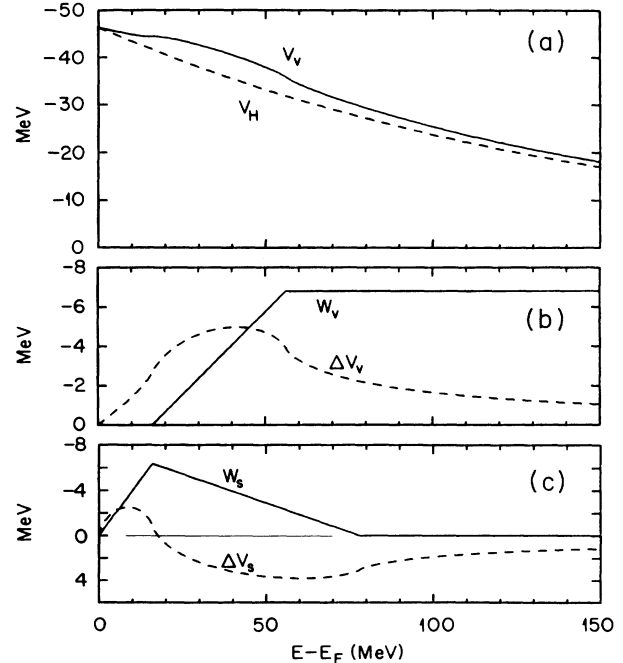


FIG. 1. The solid straight lines in the middle and lower drawings show the dependence upon $E - E_F$ ($E_F = -6$ MeV) of the quantities $W_v(E)$ and $W_s(E)$ in the mean field model of Sec. III, while the dashed curves represent the corresponding values of $\Delta V_v(E)$ and $\Delta V_s(E)$ as calculated from the DR, (2.19). The dashed curve in the upper drawing gives the Hartree-Fock depth $V_H(E)$, while the solid curve is the sum $V_H(E) + \Delta V_v(E)$.

$$\mathcal{W}_s(r;E) = -4a_s W_s(E) \frac{d}{dr} f(X_s) . \quad (2.10)$$

The mean field is real at the Fermi energy E_F ; this implies that

$$\mathcal{W}(r;E_F) = 0 . \quad (2.11)$$

We recall that the Fermi energy lies halfway between the last occupied and the first unoccupied shell in ²⁰⁸Pb. We henceforth take the numerical value

$$E_F = -6 \text{ MeV} . \quad (2.12)$$

In order to apply the DR, Eq. (1.5), one also needs $\mathcal{W}(r;E)$ for negative E . We shall make the assumption⁵ that $\mathcal{W}(r;E)$ is symmetric with respect to the Fermi energy E_F :

$$\mathcal{W}(r;E + E_F) = \mathcal{W}(r;E_F - E) . \quad (2.13)$$

This symmetry assumption is plausible because $\mathcal{W}(r;E)$ is intimately related to the time evolution of a single-particle configuration in ²⁰⁹Pb (for $E > E_F$) or in ²⁰⁷Pb (for $E < E_F$) with excitation energy $|E - E_F|$. Equation (2.13) amounts to assuming that this time evolution is approximately the same in ²⁰⁷Pb as it is in ²⁰⁹Pb, provided the excitation energy is the same. This assumption is supported by empirical evidence¹¹ as well as by theoretical calculations.¹²⁻¹⁴

In Secs. III–V we make the approximation that the parameters r_W , a_W , r_s , and a_s are independent of energy. This “constant geometry” model then involves only two functions of energy, namely the potential strengths $W_v(E)$ and $W_s(E)$. In Sec. VI we shall consider a model for which the surface geometry parameters are allowed to be energy dependent for $E < 10$ MeV. Finally, in Sec. VII we shall consider a more refined model with r_s constant but with $\mathcal{W}(r;E)$ allowed to depend on the orbital angular momentum of the projectile for $E < 12$ MeV.

D. Dispersive contribution

One consequence of Eq. (2.13) is that

$$\Delta\mathcal{V}(r;E_F) = 0 , \quad (2.14)$$

which implies that at the Fermi energy the mean field becomes identical to the Hartree-Fock contribution. This is in keeping with the fact that, in practice, the effective interaction used as input in a Hartree-Fock calculation is chosen in such a way as to reproduce the experimental value of the Fermi energy.

The main characteristic of our approach is that, except for the constant parameter α which specifies the exponential energy dependence of the Hartree-Fock component, Eq. (2.7), the energy dependence of the real part of the mean field is fully determined from the imaginary part of the mean field. Indeed, the dispersive contribution $\Delta\mathcal{V}(r;E)$ to the real part of the mean field is given by Eq. (1.5).

Equations (1.5) and (2.8) show that $\Delta\mathcal{V}(r;E)$ is the sum of a volume component $\Delta\mathcal{V}_v(r;E)$ and of a surface component $\Delta\mathcal{V}_s(r;E)$:

$$\Delta\mathcal{V}(r;E) = \Delta\mathcal{V}_v(r;E) + \Delta\mathcal{V}_s(r;E) , \quad (2.15)$$

with ($q = v, s$)

$$\Delta\mathcal{V}_q(r;E) = (P/\pi) \int_{-\infty}^{+\infty} \frac{\mathcal{W}_q(r;E')}{E' - E} dE' \quad (2.16a)$$

$$= \frac{2}{\pi} (E_F - E) \int_0^{\infty} \frac{\mathcal{W}_q(r;E' + E_F) dE'}{(E - E_F)^2 - E'^2} . \quad (2.16b)$$

In Secs. III–V we make the simple assumption that the geometrical parameters a_W , r_W , a_s , and r_s are independent of energy. Then, one has

$$\Delta\mathcal{V}_v(r;E) = \Delta V_v(E) f(X_W) , \quad (2.17)$$

$$\Delta\mathcal{V}_s(r;E) = -4a_s \Delta V_s(E) \frac{d}{dr} f(X_s) , \quad (2.18)$$

and, with ($q = v, s$)

$$\Delta V_q(E) = \frac{P}{\pi} \int_{-\infty}^{\infty} \frac{W_q(E')}{E' - E} dE' . \quad (2.19)$$

We shall parametrize each of the empirical functions $W_s(E)$ and $W_v(E)$ by a sequence of contiguous linear segments (LS's). Our reason for adopting this “LS parametrization” is that we can then evaluate the DR integral analytically.¹⁵ In Figs. 1(b) and 1(c) the solid curves illustrate LS parametrizations and the dashed curves represent the corresponding dispersive corrections calculated with the assumption of symmetry, Eq. (2.13).

Moreover, we shall assume that

$$r_W = r_H , \quad a_W = a_H . \quad (2.20)$$

Our motivation for making this assumption is that the radial shape of $\Delta\mathcal{V}_v(r;E)$ is then identical to that of the Hartree-Fock contribution. These two quantities can thus be combined into a single volume component

$$\mathcal{V}_v(r;E) = \mathcal{V}_H(r;E) + \Delta\mathcal{V}_v(r;E) \quad (2.21)$$

$$= V_v(E) f(X_H) , \quad (2.22)$$

with

$$V_v(E) = V_H(E) + \Delta V_v(E) . \quad (2.23)$$

In Fig. 1(a) the solid curve represents the sum of the potential strengths $V_H(E)$ and $\Delta V_v(E)$, which are represented by the dashed curves in Figs. 1(a) and 1(b).

In summary, our model involves the following adjustable quantities: (i) the four constants r_H , a_H , $V_H(0)$, and α which specify the Hartree-Fock field, see Eqs. (2.3) and (2.7); (ii) the radius r_s and diffuseness a_s which characterize the surface component of the imaginary part of the mean field; and (iii) the energy-dependent functions $W_v(E)$ and $W_s(E)$, which are also defined by a few constants. These quantities will be determined in Sec. III from analyses of the many experimental scattering data in the energy domain $4 < E < 150$ MeV. The accuracy of the model will be tested by the following two criteria: (a) the quality of the fits to these experi-

mental scattering data, and (b) the agreement between the experimental energies and wave functions of the bound single-particle states and the model values obtained from the extrapolation of $\mathcal{V}(r;E)$ into the negative energy domain. This extrapolation will be discussed in Sec. IV; it will be done analytically and involves no further adjustment of parameters.

We show in Secs. III and IV that our model nicely satisfies these two criteria. We emphasize that this is by no means trivial. Indeed, we shall see in Sec. V that the energy dependence of $\mathcal{V}(r;E)$ is rather intricate at small negative and positive energies. This intricate energy dependence is a prediction of the DR, as illustrated in Fig. 1; it will be shown to yield detailed agreement with the experimental data. These data span a large energy domain extending from negative (-20 MeV) to positive ($+165$ MeV) energies. It is quite remarkable that the good agreement between our model and these numerous experimental data is achieved by adjusting only a few constants and by determining two smooth functions of the energy, namely $W_v(E)$ and $W_s(E)$.

III. ANALYSIS OF THE EXPERIMENTAL SCATTERING DATA

A. The experimental data

We shall determine the parameters of our model by fitting the following experimental scattering data, which will be displayed below.

(a) Differential elastic scattering cross sections at 17 energies between 4 and 40 MeV.

(b) Analyzing power measurements at 10 and 14 MeV.

(c) Total $n + {}^{208}\text{Pb}$ cross section from 1 to 25 MeV and $n + {}^{\text{nat}}\text{Pb}$ cross section from 2 to 120 MeV.

To perform least-squares fits on the 17 differential elastic angular distributions we use the computer code GENOA,¹⁶ with modifications to make the real and imaginary volume geometries the same, Eq. (2.20), and to include a real surface contribution of Woods-Saxon derivative shape. At each energy the total cross section will be included with an artificially small uncertainty, $\pm 0.1\%$, to give it a non-negligible weight relative to the many points in the scattering distributions. The same weighting procedure was used in Ref. 2. Table I lists the 17 to-

TABLE I. Total cross section^a for $n + {}^{208}\text{Pb}$ at selected energies.

E (MeV)	σ_T (b)	E (MeV)	σ_T (b)
4.0	7.90	11.0	5.16
4.5	7.80	14.0	5.46
5.0	7.55	20.0	5.90
5.5	7.18	22.0	5.83
6.0	6.62	24.0	5.72
6.5	6.22	25.7	5.62
7.0	5.94	30.3	5.18
9.0	5.28	40.0	4.45
10.0	5.20		

^aEstimated uncertainties of $\pm 0.5\%$ for $E < 25$ MeV and $\pm 1.0\%$ for $E > 25$ MeV. Artificial uncertainties of $\pm 0.1\%$ used for weighting in the least-squares searches.

tal cross sections as deduced from smooth curves drawn through the data to be presented in Sec. III E; the experimental uncertainties are discussed in the Appendix. At 10 and 14 MeV we also include the analyzing power data. For calculating and plotting the total cross sections as a function of energy we use the code SCAT,¹⁷ with the appropriate modifications.

In addition, we shall require that the energies of the $3p_{1/2}$ and $2g_{9/2}$ single-particle bound states in the Hartree-Fock potential \mathcal{V}_H lie on opposite sides of the Fermi energy E_F , in order to ensure that the mean field approximately reproduces the Fermi energy; we recall in this respect that $\mathcal{V}(r;E_F)$ is identical to $\mathcal{V}_H(r;E_F)$, see Eq. (2.14). We shall also compare predicted bound state energies from the model with energies of the known particle and hole states. For computing bound state energies and wave functions we will use the code DENS,¹⁸ modified to include a real surface contribution.

Finally, we shall compare the predictions of the model with the energy-averaged scattering functions for individual neutron partial waves, particularly for s waves, as derived from the analysis of high resolution elastic scattering neutron cross sections below 1 MeV.^{19,20}

B. Search of the geometrical parameters of the fixed geometry model

In order to determine the geometrical parameters we first made a series of multiparameter optical model fits to the experimental differential elastic angular distributions.^{2-4,21-24} In these preliminary searches, for reasons to be discussed in Secs. VI and VII, we emphasized the data for $E > 12$ MeV. Good starting values were provided by the ‘‘common geometry’’ deduced by Finlay *et al.*² from phenomenological analyses of data from 7 to 40 MeV. They found $a_v = 0.685$ fm, $r_s = 1.283$ fm, and $a_s = 0.569$ fm. We adopt very similar values. For the diffuseness of the real and imaginary volume potentials we henceforth take

$$a_H = a_W = 0.68 \text{ fm} , \quad (3.1)$$

and for the parameters r_s and a_s , which characterize the shape of the surface absorption, we take

$$r_s = 1.27 \text{ fm} , \quad a_s = 0.58 \text{ fm} . \quad (3.2)$$

Later, in Secs. VI and VII, we allow the surface geometry to be energy dependent for $E < 10$ MeV to achieve better fits to the data. A similar procedure was followed in the original analysis⁴ of these data.

For the real volume radius r_H we found a value somewhat different from the radius r_v of Ref. 2. That is an expected consequence of including a real surface term.⁶ Using the geometries given in Eqs. (3.1) and (3.2), we found that r_H must be chosen quite precisely, i.e., to ± 0.003 fm, to allow the phenomenological surface depth ΔV_s to be consistent with that predicted by the DR for $E \geq 14$ MeV. Henceforth we take

$$r_H = r_W = 1.240 \text{ fm} . \quad (3.3)$$

There would be no significant changes in the quality of

fits or in our conclusions if we were to increase a_H to 0.70 fm (i.e., the value used in Ref. 4), and reduce r_H to 1.225 fm.

C. Depth of the volume contribution

Henceforth (except in Secs. VI and VII), all the geometrical parameters are kept fixed at the values given in Eqs. (3.1)–(3.3). We first fit the experimental angular distributions at 17 energies ranging from 4 to 40 MeV considering four parameters as adjustables, namely the potential strengths W_v , W_s , ΔV_s , and V_v . Here, V_v is the depth of the volume component of the real part of the mean field, see Eq. (2.23). The values of W_v and V_v determined by these least squares fits are represented by the solid symbols in Fig. 2. The empirical values of W_v are seen to lie close to the following linear approximation,

$$W_v(E) = -0.17(E - 10) \text{ MeV for } 10 < E < 50 \text{ MeV}, \quad (3.4a)$$

which is represented by the solid line in Fig. 2(a).

In order to apply the DR, Eq. (2.19), one needs the value of $W_v(E)$ for E larger than 40 MeV. In this higher energy domain, one can use empirical information provided by the total cross section. Near 80 MeV the cross section has a maximum²⁵ which requires

$W_v \approx -7$ MeV. Hence, we parametrize $W_v(E)$ by the linear expression (3.4a) up to $E = 50$ MeV, beyond which we take the constant value

$$W_v(E) = -6.8 \text{ MeV for } E > 50 \text{ MeV}. \quad (3.4b)$$

Equations (3.4a) and (3.4b) are represented by the solid lines in Fig. 1(b).

From the LS approximation, Eqs. (3.4a) and (3.4b), and the DR, Eq. (2.19), one obtains the values of $\Delta V_v(E)$ represented by the dashed curves in Fig. 2(a) and in Fig. 1(b). Equation (2.23) shows that to obtain the Hartree-Fock depth V_H one should subtract the quantity ΔV_v from the full depth V_v . This subtraction yields the values represented by the open symbols in Fig. 2(b). The dashed curves in Figs. 2(b) and 1(a) represent the following exponential parametrization, see Eq. (2.7):

$$V_H(E) = -46.4 \exp[-0.31(E - E_F)/46.4], \quad (3.5a)$$

which, at energies near the Fermi surface, gives the approximation

$$V_H(E) \approx -46.4 + 0.31(E - E_F). \quad (3.5b)$$

In this parametrization, the depth of the Hartree-Fock potential at the Fermi energy is -46.4 MeV. This numerical value has been determined, in part, by our requirement that the binding energies of the $3p_{1/2}$ and $2g_{9/2}$ single-particle states should lie on opposite sides of the Fermi energy. Equation (3.5a) is equivalent to setting $\alpha = 0.0067 \text{ MeV}^{-1}$ in Eq. (2.7). This corresponds to a nonlocality range $\beta = 0.74$ fm, in fair agreement with the phenomenological value $\beta = 0.85$ fm assumed by Perey and Buck in their pioneering work.¹⁰

The solid curve in Fig. 2(b) [also Fig. 1(a)] represents the potential $V_v(E)$ which is the sum, Eq. (2.23), of the potentials $V_H(E)$ and $\Delta V_v(E)$ represented by the dashed curves in Figs. 2(b) and 2(a) [also Figs. 1(a) and 1(b)]. The fact that $V_v(E)$ is approximately independent of energy between 5 and 15 MeV is seen to be a consequence of the DR prediction that the dispersive volume contribution $\Delta V_v(E)$ increases especially rapidly in that region. We emphasize that $\Delta V_v(E)$ is fully determined by the DR, Eq. (2.19), once $W_v(E)$ is known. The empirical V_v represented by the solid points in Fig. 2(a) deviate upward from the prediction. In Sec. VII we show that this deviation is probably a consequence of our overly simple model for the surface imaginary potential $\mathcal{W}_s(r; E)$ for $E < 12$ MeV, and we construct a more refined model which improves the fits to the data and results in empirical V_v which lie very close to the predicted curve of $V_v(E)$.

D. Strength of the surface-peaked contribution

We now turn to the strength of the surface-peaked contributions to the real and imaginary parts of the mean field for the fixed-geometry model. We fix W_v and V_v at the values represented by the solid curves in Fig. 2, and perform least square fits to the experimental cross sections with only two adjustable parameters, namely ΔV_s and W_s . The resulting values are represented by

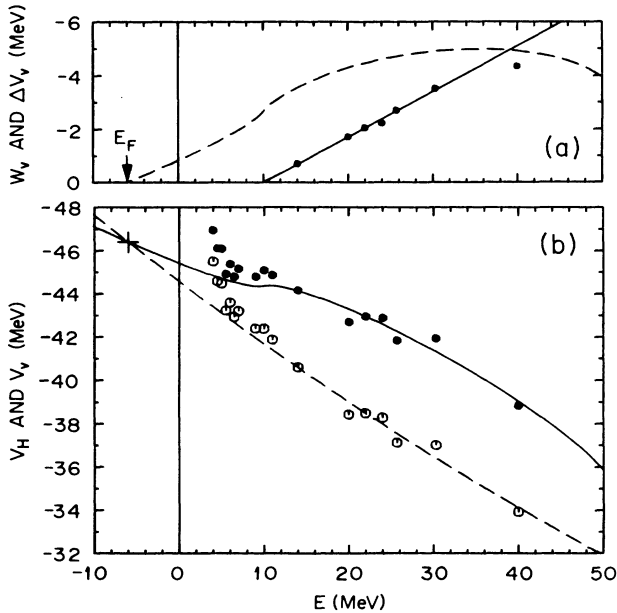


FIG. 2. The dots represent the empirical values of W_v and of V_v determined by least squares fits to the experimental data. In the upper drawing, (a), the solid line gives the linear approximation of $W_v(E)$, while the dashed line shows the corresponding $\Delta V_v(E)$ as obtained from the DR. The open symbols in the lower drawing, (b), represent the values of the difference $V_H = V_v - \Delta V_v$; the dashed line is the exponential approximation to the Hartree-Fock depth $V_H(E)$, while the solid curve is the sum $V_H(E) + \Delta V_v(E)$. The cross at $E = -6$ MeV represents V_H at the Fermi energy E_F .

the dots in Fig. 3. The values of W_s are in close agreement with the following LS parametrization (W_s in MeV),

$$W_s(E) = -0.4(E - E_F) \quad \text{for } -6 < E < 10 \text{ MeV}, \quad (3.6a)$$

$$W_s(E) = 0.103(E - 72) \quad \text{for } 10 < E < 72 \text{ MeV}, \quad (3.6b)$$

and

$$W_s(E) = 0 \quad \text{for } E > 72 \text{ MeV}; \quad (3.6c)$$

this LS parametrization is represented by the solid lines in Figs. 3(a) and 1(c).

In Fig. 3 the open symbols represent the W_s required to describe the average scattering functions which were deduced^{19,20} for the neutron partial waves $s_{1/2}$, $p_{1/2}$, $p_{3/2}$, $d_{3/2}$, and $d_{5/2}$ from high resolution measurements of the total cross section for 0.05- to 1-MeV neutrons. These values have large uncertainties, about $\pm 50\%$, because they are determined essentially by summing reduced neutron widths of only a few resonances. They are included here only to demonstrate consistency with the decreasing lower segment of the LS parametrization.

From this LS parametrization and the DR, Eq. (2.19),

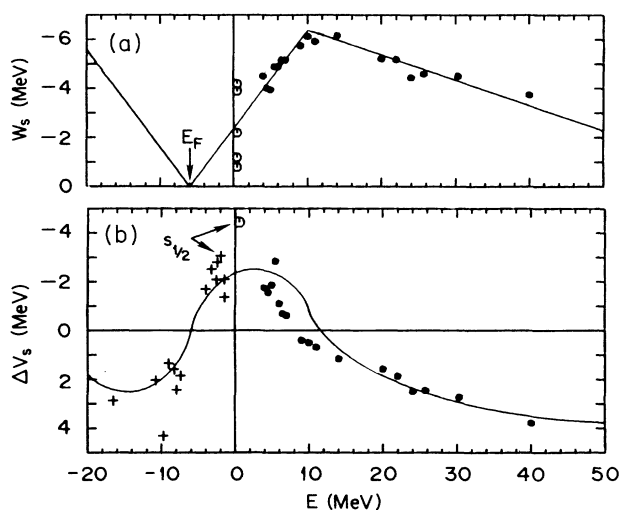


FIG. 3. Energy dependence of the strengths of the surface-peaked components of the imaginary and real parts of the optical-model potential. The solid points are obtained from fits to the experimental cross sections, with the geometrical parameters in Eqs. (3.1)–(3.3) and taking the strengths of the volume components from the solid curves shown in Fig. 2. The values of W_s are presented in (a), in which the LS is a visual fit. When inserted in the DR the LS yields the values of ΔV_s shown by the solid curve in (b). The solid dots in (b) represent the empirical values of ΔV_s obtained from individual fits. The crosses are empirical values of ΔV_s required to reproduce the experimental single-particle energies. The open symbols in (a) show the values of W_s required to describe the average scattering functions for 0.05- to 1-MeV neutrons; the five symbols in order of increasing $|W_s|$ correspond to $p_{1/2}$, $p_{3/2}$, $d_{3/2}$, $s_{1/2}$, and $d_{5/2}$ partial waves. In (b) the open symbol represents the corresponding ΔV_s for $s_{1/2}$ and the cross at the end of the arrow indicates the $4s_{1/2}$ bound state.

we calculate the corresponding function $\Delta V_s(E)$, which is represented by the solid curve in Fig. 3(b) or the dashed curve in Fig. 1(c). This curve closely follows the empirical values of ΔV_s that were obtained from the individual fits and are represented by the solid points in Fig. 3(b). This agreement demonstrates that the data are well described by the DR model. This is further illustrated by the general agreement between the predicted DR curve in Fig. 3 and the surface depths (crosses) required to reproduce experimental single-particle energies (see Sec. IV). The calculated curve is also consistent with the open symbol, which represents the potential required to fit the nonresonance s -wave cross section (or, equivalently, the real part of the energy-averaged s -wave scattering function) for neutrons in the energy range 0.05–1 MeV.^{19,20} In Sec. IV we shall also show that the asymptotic values of the single-particle wave functions are in excellent agreement with experimental values deduced from sub-Coulomb pickup reactions.

For $E \geq 14$ MeV the empirical ΔV_s in Fig. 3(b) follow the DR prediction particularly well; that would not be the case if the Hartree-Fock parameters were not well chosen. In Sec. V we discuss the relationship of ΔV_s to the Hartree-Fock radius r_H . If we were to change r_H even slightly, say from 1.240 to 1.243 fm, without readjusting other constants, the empirical ΔV_s would be falsely adjusted to compensate for the inadequacy of those parameters. Likewise, an assumption of an energy dependence in r_H for $E \geq 14$ MeV would require a compensating energy dependence, say in the imaginary radius r_W , to allow ΔV_s to follow the DR prediction. A related phenomenon is present for the energies $4 \leq E \leq 11$ MeV. Those empirical points for ΔV_s do not closely follow the DR prediction because they have been somewhat falsely adjusted in the fitting procedures in an attempt to compensate for the inadequacies in that domain of our simple “fixed geometry” model for $\mathcal{W}(r; E)$. We return to the latter problem in Secs. VI and VII.

E. Comparison with the experimental cross sections in the energy domain $1 < E < 165$ MeV

We now compare the experimental cross sections with those calculated from our optical-model potential. The geometrical parameters of the model are specified by Eqs. (3.1)–(3.3). The strengths of the various components are specified by Eqs. (3.4a), (3.4b), (3.6a)–(3.6d), and the DR, (2.19). They are represented by the curves shown in Figs. 1–3. We again emphasize that the DR fully determines the real part of the dispersive contribution once the imaginary part of the mean field is specified.

The solid curves in Fig. 4 represent the differential cross sections calculated from our model in the energy domain $14 \leq E \leq 40$ MeV. The agreement with the data,^{2,21–23} which are represented by the dots, is quite similar to that shown in Fig. 5 of Ref. 2, where a purely phenomenological optical-model potential was used. The χ^2/N deduced by comparison of the curves to the data are listed in column 2 of Table II. The predicted

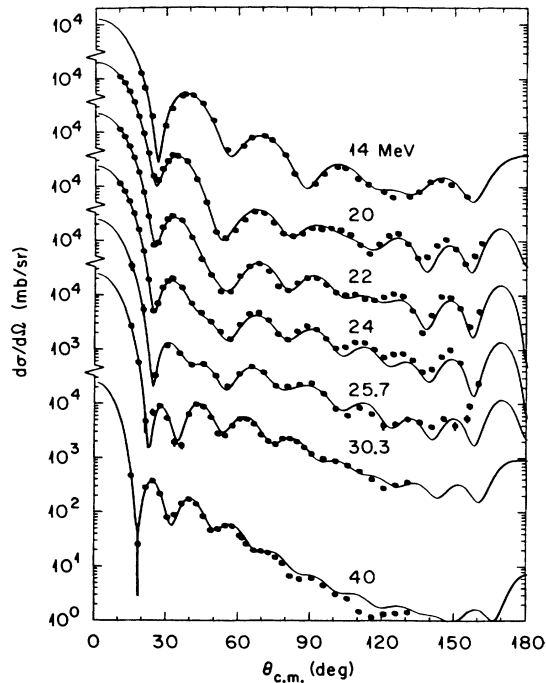


FIG. 4. The dots give the experimental differential cross sections at the energies indicated. The curves are calculated from the model described in Sec. III.

total cross sections average 0.4% less than the values in Table I.

Figure 5 shows the comparison between the experimental^{23,24} analyzing power at 10 and 14 MeV and the predictions of our model. The agreement is quite good

TABLE II. χ^2/N from comparison of model predictions to experimental angular distributions for N scattering angles at the energy E .

E (MeV)	Fixed geometry ^a	$r_s(E)$ and $a_s(E)$ ^b	$a_s(E)$ and l dependent ^c
4.0	4.7	11.5	3.2
4.5	9.1	6.6	6.4
5.0	11.9	6.2	6.4
5.5	13.3	11.8	14.6
6.0	43.8	17.6	11.6
6.5	54.7	25.2	5.5
7.0	47.0	26.6	6.9
9.0	36.4	33.6	15.6
10.0	20.2	20.2	9.0
11.0	11.6	11.7	11.4
14.0	12.0		
20.0	9.4		
22.0	7.0		
24.0	13.8		
25.7	4.8		
30.3	10.4		
40.0	17.6		

^aSee Sec. III.

^bSee Sec. VI.

^cSee Sec. VII.

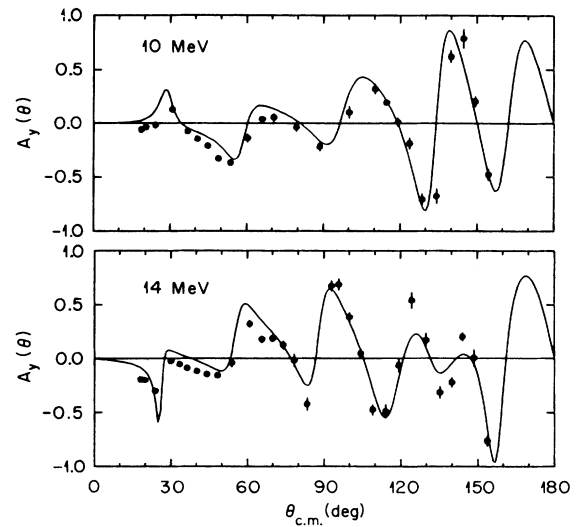


FIG. 5. Comparison between the experimental (Refs. 23 and 24) analyzing powers at 10 and 14 MeV and the predictions of the fixed geometry model.

in view of the fact that these data were given relatively little weight in our analysis; it could be improved by slightly readjusting the spin-orbit parameters.

In Fig. 6 the dashed curves show the differential cross sections calculated from our model for the energy domain $4 \leq E \leq 11$ MeV, and the points are the experi-

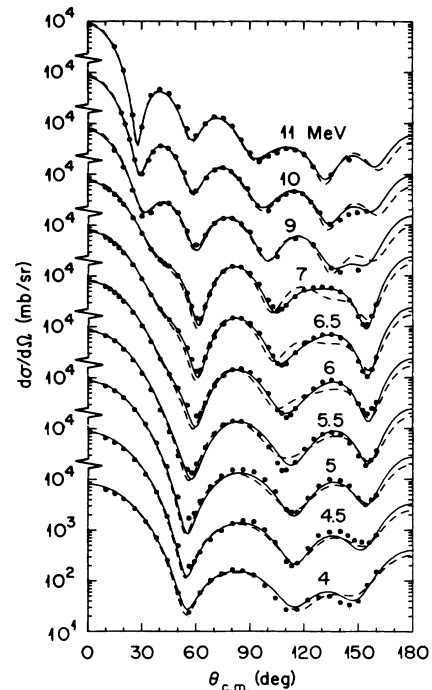


FIG. 6. The dots give the experimental differential cross sections for 7, 9, 10, and 11 MeV and the shape elastic part of the experimental differential cross sections at 4, 4.5, 5, 5.5, 6, and 6.5 MeV. The dashed curves have been calculated from the model described in Sec. III. The solid curves correspond to an angular-momentum dependence in the strength and an energy dependence in the diffuseness of the imaginary potential (Sec. VII).

mental values. For $E < 7$ MeV the points represent shape elastic cross sections²⁶ that were deduced in Ref. 4 by subtracting calculated compound elastic cross sections from the total elastic values. Column 2 of Table II lists the χ^2/N deduced by comparison of the data to the curves. It is seen that our model yields good agreement with the data except at the larger angles (i.e., $\theta_{c.m.} > 100^\circ$). The poorer agreement for these larger angles will be discussed in detail in Secs. VI and VII.

In Fig. 7 the predicted total cross sections for neutron energies up to 25 MeV are compared with the data. The points represent energy averages of cross sections that were measured during a previously reported experiment^{19,20} and are presented here for the first time for $E > 1$ MeV. Comparisons to previous experiments and a discussion of experimental uncertainties are given in the Appendix. The dashed curve corresponds to our present model, while the solid curve is associated with a refined model (Sec. VII) in which the surface potentials are angular-momentum dependent for $E < 12$ MeV. For $E > 12$ MeV the models, and the curves in the figure, are practically identical.

In Fig. 8 our model predictions of total cross sections for $n + {}^{208}\text{Pb}$ are compared with measured cross sections for $n + {}^{\text{nat}}\text{Pb}$ for energies up to 120 MeV. The solid and dashed notations are the same as for Fig. 7. The energy-averaged cross sections for ${}^{\text{nat}}\text{Pb}$ and ${}^{208}\text{Pb}$ are expected to be nearly the same, to within 1%, because the atomic weights are nearly identical (see Appendix). In Fig. 8(a) the points represent values that we deduced by energy averaging cross sections that had been measured^{27,28} with good energy resolution by time-of-flight methods. In Fig. 8(b) the points for $15 < E < 120$ MeV are from Ref. 25, except that we have renormalized the authors' energy scale by 1.06, as discussed in the Appendix.

Our model is seen to give a good description of the total cross section over a broad energy range which ex-

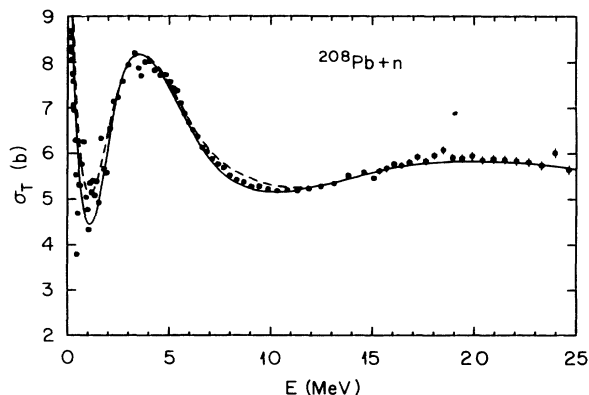


FIG. 7. Energy dependence of the total $n + {}^{208}\text{Pb}$ cross section below 25 MeV. The dots are previously unpublished values which use the experimental setup described in Refs. 19 and 20. The dashed curve (and the solid curve above 12 MeV) corresponds to the model described in Sec. III. The solid curve below 12 MeV is associated with the same imaginary potential as for the solid curves in Fig. 6 (Sec. VI).

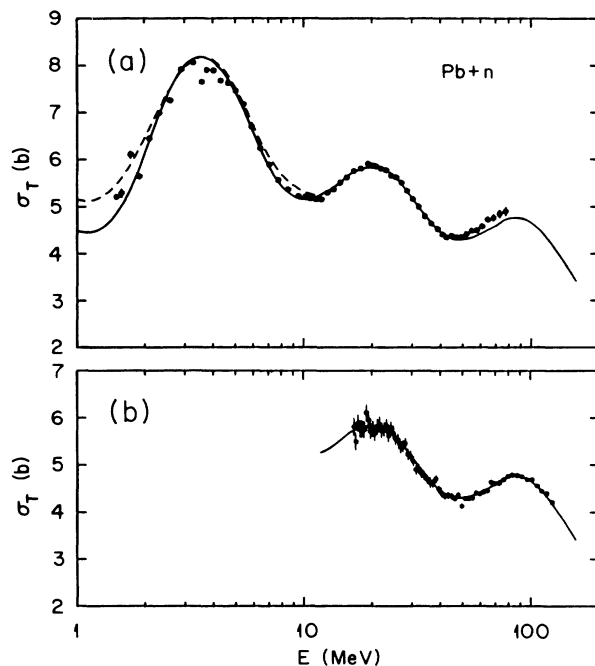


FIG. 8. Energy dependence of the total $n + {}^{\text{nat}}\text{Pb}$ cross section. In (a) the points represent energy averages of the experimental cross sections from Refs. 27 and 28. In (b) the points represent the experimental cross sections from Ref. 25, but are plotted at energies of 1.06 times those quoted by the authors. The justification for this renormalization is given in the Appendix. The curves have the same meaning as in Fig. 7.

tends up to 120 MeV. Furthermore, it is consistent with unpublished²⁹ $n + {}^{208}\text{Pb}$ total cross sections for energies up to 165 MeV. The agreement in magnitude with the experimental valley and peak for $E > 50$ MeV in Fig. 8 shows that $\mathcal{W}(r;E)$ is a good approximation [see Eq. (3.4b)]. Furthermore, the agreement in energies for the peak and valley shows the correctness of the exponential energy dependence for $V_H(E)$; although a linear dependence for $V_H(E)$ could have been assumed if the analysis were restricted to $E < 40$ MeV, an extrapolation to higher energies of such a linear parametrization would not have yielded the correct energy for the peak near 80 MeV.

IV. EXTRAPOLATION TOWARDS NEGATIVE ENERGIES

The average potential $\mathcal{V}(r;E)$ is a continuous function of E which varies smoothly when E changes sign; for $E > 0$ it is the real part of the optical-model potential and for $E < 0$ it is the shell-model potential. The fact that empirical data from all energies are utilized for parametrizing $\mathcal{V}(r;E)$ is especially useful for the shell model because the few data available from the domain of $E < 0$ are strongly augmented by the abundant and varied scattering data from $E > 0$. Essentially, the information from $E < 0$ reduces to the energies of the single-particle bound states and to the asymptotic value of some single-particle wave functions at large dis-

tances.^{30–33} For our model, in fact, the only datum utilized from $E < 0$ was the centroid energy for the valence orbits or, equivalently, the Fermi energy. We now calculate the single-particle energies and wave functions from our model and compare with the experimental values. Furthermore, we compare the predicted and experimental spreading widths for the deep $1h_{11/2}$ hole state; and we predict spectroscopic factors, occupation numbers, and rms radii for the valence orbits.

A. Single-particle energies

The experimental values of the neutron single-particle energies in ²⁰⁸Pb are tabulated in Table III. They are taken from Refs. 34 and 35 in the case of the two valence shells ($-12 \text{ MeV} < E < 0$), and from Ref. 36 in the case of the $1h_{11/2}$ deeply bound state; the latter is spread over an energy interval of about 3 MeV (see Fig. 4.41 of Ref. 14).^{37,38} Table III also contains the average energy of the particle (p) and hole (h) valence shells, as defined by

$$\langle E_p \rangle = \sum_{\text{uno}} (2j+1) E_{nlj} / \sum_{\text{uno}} (2j+1), \quad (4.1a)$$

$$\langle E_h \rangle = \sum_{\text{occ}} (2j+1) E_{nlj} / \sum_{\text{occ}} (2j+1), \quad (4.1b)$$

where uno and occ refer to the subshells of the normally unoccupied and occupied valence shells.

We consider the following two methods in order to compare the experimental single-particle energies to those predicted by our model: (i) In keeping with the procedure used in Fig. 3, we take the value of $V_v(E_{nlj})$

TABLE III. Neutron single-particle energies E_{nlj} in ²⁰⁸Pb. The left-hand column specifies the principal, orbital, and total angular momentum quantum numbers, the column labeled \mathcal{V}_H contains the Hartree-Fock values, that labeled \mathcal{V}_v gives values with only the dispersive volume correction added to the Hartree-Fock field, that labeled $\mathcal{V}_v + \Delta\mathcal{V}_s$ gives the values calculated from our full model potential, and that labeled Expt. lists the experimental values. Also listed are averages for the valence shells. All energies are in MeV.

nlj	\mathcal{V}_H	\mathcal{V}_v	$\mathcal{V}_v + \Delta\mathcal{V}_s$	Expt.
$3d_{3/2}$	-0.37	-0.72	-1.40	-1.40
$2g_{7/2}$	-0.32	-0.82	-1.75	-1.44
$4s_{1/2}$	-0.79	-1.07	-1.62	-1.90
$3d_{5/2}$	-1.04	-1.41	-2.08	-2.37
$1j_{15/2}$	-0.78	-1.36	-2.39	-2.51
$1i_{11/2}$	-1.46	-2.00	-2.80	-3.16
$2g_{9/2}$	-2.88	-3.20	-3.81	-3.94
$\langle E_p \rangle$	-1.22	-1.68	-2.50	-2.63
$3p_{1/2}$	-8.40	-8.14	-7.64	-7.37
$2f_{5/2}$	-9.37	-8.98	-8.33	-7.94
$3p_{3/2}$	-9.27	-8.90	-8.30	-8.26
$1i_{13/2}$	-10.14	-9.63	-8.85	-9.00
$2f_{7/2}$	-12.18	-11.42	-10.56	-9.71
$1h_{9/2}$	-12.33	-11.48	-10.74	-10.78
$\langle E_h \rangle$	-10.75	-10.15	-9.41	-9.25
$1h_{11/2}$	-19.51	-17.58	-16.66	-16.5±0.5

from the solid curve in Fig. 2(b); we then adjust the strength $\Delta\mathcal{V}_s(E_{nlj})$ of the surface component so that the full potential $\mathcal{V}_v(r;E_{nlj}) + \Delta\mathcal{V}_s(r;E_{nlj})$ yields the experimental single-particle energies. The corresponding values of $\Delta\mathcal{V}_s(E_{nlj})$ are represented by crosses in Fig. 3(b). These are seen to lie close to the solid curve, i.e., to the prediction of our DR model. (ii) We calculate the energies of the bound single-particle states in the full potential $\mathcal{V}(r;E)$ of our model. The results are listed in Table III and plotted in Fig. 9. One sees that the dispersive corrections bring the calculated values into close agreement with the experimental energies. In particular, the particle-hole gap as measured by the difference $\delta_{\text{ph}} = \langle E_p \rangle - \langle E_h \rangle$ is reduced from 9.53 MeV in the Hartree-Fock approximation to 6.91 MeV in the full potential; the latter compares quite well with the experimental value $\delta_{\text{ph}} = 6.62 \text{ MeV}$. The agreement between our calculated single-particle energies and the experimental values is better than achieved in any of the microscopic calculations which are surveyed in Ref. 14.

Also listed in Table III and plotted in Fig. 9 are the bound state energies in the field $\mathcal{V}_v(r;E)$, which includes only the sum of the dispersive volume correction plus the Hartree-Fock field. The corresponding particle-hole gap is 8.47 MeV. By comparison to the gaps derived from the Hartree-Fock field and from the full field, we see that, on average, about 40% of the total correction

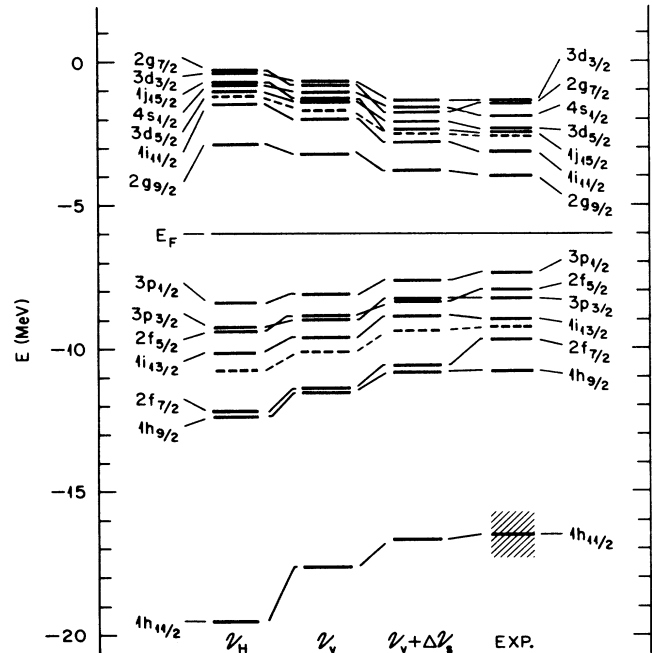


FIG. 9. Neutron single-particle energies in ²⁰⁸Pb. The first column at the left gives the Hartree-Fock values, the second column those calculated with the volume correction added to the Hartree-Fock potential, the third column those calculated from the full potential, and the right-hand column the experimental values. The dashed lines represent the particle and hole averages defined by Eq. (4.1): $\langle E_p \rangle$ for $E > E_F$ and $\langle E_h \rangle$ for $E < E_F$.

results from volume dispersive effects and about 60% from the surface correction $\Delta\mathcal{V}_s$. We recall that the volume correction results entirely from the imaginary potential at relatively distant energies, $|E - E_F| > 16$ MeV; accordingly, $V_v(E)$ is almost a linear function of E in the vicinity of the Fermi energy:

$$V_v(E) \simeq -46.4 \text{ MeV} + 0.17(E - E_F). \quad (4.2)$$

In contrast, the surface term $\Delta V_s(E)$ is strongly influenced by $W_s(E)$ at energies $|E - E_F| < 16$ MeV, and therefore varies rapidly with E in the vicinity of E_F .

We note that the good agreement between our model and experiment extends to the energy (-16.5 MeV) of the deeply bound $1h_{11/2}$ single-particle neutron orbit, which the microscopic calculations overbind by about 2 MeV.¹⁴ The spreading width Γ^\downarrow for the $1h_{11/2}$ neutron orbit can be estimated from the expression

$$\Gamma^\downarrow \approx 2 \int u_{1h_{11/2}}^2(r) \mathcal{W}(r; E_{1h_{11/2}}) dr, \quad (4.3)$$

where $u_{1h_{11/2}}(r)/r$ is the $1h_{11/2}$ radial wave function in the full potential $\mathcal{V}(r; E)$. The wave function is normalized;

$$\int [u_{nlj}(r)/r]^2 r^2 dr \equiv \int u_{nlj}^2(r) dr = 1. \quad (4.4)$$

This yields $\Gamma^\downarrow = 2.7$ MeV, which is in reasonable agreement with the reported experimental value³⁷ $\Gamma^\downarrow = 3.7 \pm 0.5$ MeV. A better evaluation of Γ^\downarrow should take into account the fact that the microscopic HF field is nonlocal.^{39,40} By noting that Γ^\downarrow is connected to the lifetime τ of a hole state by $\Gamma^\downarrow = \hbar/\tau$, Eqs. (1), (16), and (21) of Ref. 39 lead to the following improved approximation for Γ^\downarrow :

$$\Gamma^\downarrow = 2 \int u_{1h_{11/2}}^2(r) \mathcal{W}(r; E_{1h_{11/2}}) [m/m^*(r; E_{1h_{11/2}})] dr, \quad (4.5)$$

where $m^*(r; E)$ is the effective mass:

$$\frac{m^*(r; E)}{m} = 1 - \frac{d}{dE} \mathcal{V}(r; E). \quad (4.6)$$

The improved approximation (4.5) yields $\Gamma^\downarrow = 3.3$ MeV, in excellent agreement with the experimental value.

B. Effective masses

The energy dependence of the full potential can be characterized by the effective mass $m^*(r; E)$ which is defined by Eq. (4.6). Figure 6 of Ref. 15 shows that in our LS parametrization the effective mass becomes infinite at the energies at which linear segments meet, in particular at the Fermi energy. This is why in Fig. 10 we show it at the energy $\langle E_h \rangle = -9.41$ MeV, i.e., $E_F - 3.41$ MeV, which corresponds to the calculated centroid energy of the hole valence shell (Table III). It is seen that $m^*(r; \langle E_h \rangle)$ has a peak at the nuclear surface. The surface peaking of $m^*(r; E)$ is due to the coupling of the Hartree-Fock single-particle states to low-lying surface excitations of the ²⁰⁸Pb core.⁵ The effective

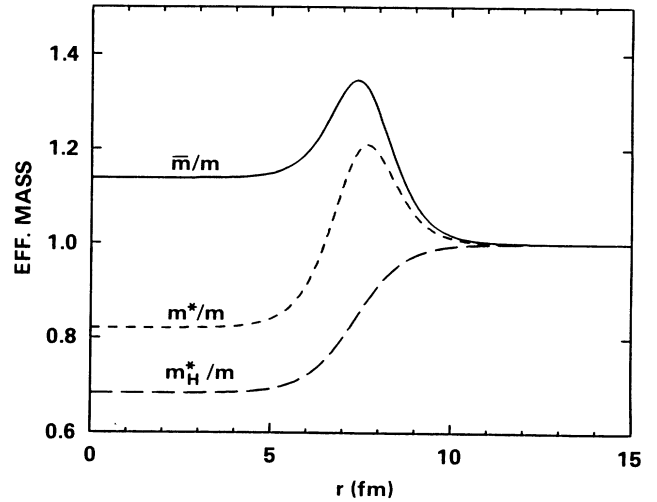


FIG. 10. Radial dependence of the effective masses at the calculated centroid energy $\langle E_h \rangle = -9.41$ MeV of the valence hole states. The short-dashed curve represents m^*/m , the long-dashed curve m_H^*/m , and the solid curve \bar{m}/m .

mass at the nuclear center only weakly depends upon energy, since approximation (4.2) yields

$$\frac{m^*(r=0; E)}{m} \simeq 0.83 \quad (4.7)$$

for E close to E_F . In contrast, the effective mass at the nuclear surface is a rather strong function of energy.⁵

In the Hartree-Fock approximation, the effective mass reduces to $m_H^*(r; E)$, where

$$\frac{m_H^*(r; E)}{m} = 1 - \frac{d}{dE} \mathcal{V}_H(r; E). \quad (4.8)$$

Equations (2.3) and (3.5b) show that in our model and in the vicinity of the Fermi energy this quantity is approximately independent of energy and is given by

$$\frac{m_H^*(r; E)}{m} = 1 - 0.31f(X_H); \quad (4.9)$$

it is represented by the long-dashed line in Fig. 10.

In the absence of dispersive correction one would have $m^*(r; E) = m_H^*(r; E)$. The “ E mass” \bar{m} defined⁴¹ by

$$\frac{\bar{m}(r; E)}{m} = 1 - \frac{d}{dE} \Delta \mathcal{V}(r; E) \quad (4.10)$$

characterizes the importance of the dispersive contribution. It is symmetric about E_F . For E close to E_F , the quantity \bar{m}/m is intimately related to the spectroscopic factor,¹⁴ as will be recalled below. Figure 10 shows that $\bar{m}(r; \langle E_h \rangle)$ is strongly peaked at the nuclear surface. This is in keeping with microscopic calculations.¹²

C. Single-particle wave functions and spectroscopic factors

We pointed out in Sec. IIB that the energy dependence of $\mathcal{V}_H(r; E)$ derives from the fact that \mathcal{V}_H is the

local equivalent of a nonlocal microscopic Hartree-Fock mean field $\mathcal{V}_H(\mathbf{r}, \mathbf{r}')$. These two fields are equivalent in the sense that they have the same single-particle energies and scattering phase shifts. However, their eigenstates are not identical: their radial parts are related by

$$\bar{u}_H(r; E) = C(E) [m_H^*(r; E)/m]^{1/2} u_H(r; E), \quad (4.11)$$

where $C(E)$ is a normalization factor. The square root on the right-hand side is often called the ‘‘Perey damping factor.’’^{10,42} Equation (4.11) holds exactly in the case of the Skyrme-Hartree-Fock approximation.⁷

In the DR approach it is assumed that the main source of nonlocality of the full mean field $\mathcal{V}(r; E)$ lies in its Hartree-Fock component, and that the dispersion correction is local.⁵ Accordingly, it appears plausible to assume that the following relation connects the eigenstate, $\bar{u}(r; E)$, of the full microscopic mean field to that, $u(r; E)$, of its local equivalent $\mathcal{V}(r; E)$:

$$\bar{u}(r; E) = C(E) [m_H^*(r; E)/m]^{1/2} u(r; E). \quad (4.12)$$

The normalization factor $C(E)$ is equal to unity in the case of scattering states. For a bound single particle state, $C(E_{nlj})$ is determined by the requirement that $\bar{u}(r; E_{nlj})$ and $u(r; E_{nlj})$ are each normalized, Eq. (4.4). The value of $m_H^*(r; \langle E_n \rangle)$ as plotted in Fig. 10 implies that

$$\bar{u}_{nlj}^2(r) < u_{nlj}^2(r) \quad \text{for small } r, \quad (4.13a)$$

where

$$\bar{u}_{nlj}(r) = \bar{u}_{nlj}(r; E_{nlj}) \quad \text{and} \quad u_{nlj}(r) = u_{nlj}(r; E_{nlj}). \quad (4.13b)$$

Since $\bar{u}_{nlj}(r)$ and $u_{nlj}(r)$ are both normalized, the inequality (4.13a) implies that

$$\bar{u}_{nlj}^2(r) > u_{nlj}^2(r) \quad \text{for large } r. \quad (4.13c)$$

This effect was pointed out by Negele.⁴³ It will be exhibited in Table IV below.

The contribution of a single-particle orbit to the neutron density distribution is given by

$$\bar{\rho}_{nlj}(r) = \frac{2j+1}{4\pi} \left[\frac{\bar{u}_{nlj}(r)}{r} \right]^2, \quad (4.14a)$$

with the following normalization:

$$\int \bar{\rho}_{nlj}(r) 4\pi r^2 dr = 2j+1. \quad (4.14b)$$

The calculated values of $\bar{\rho}_{nlj}(r)$ and of

$$\rho_{nlj}(r) = \frac{2j+1}{4\pi} \left[\frac{u_{nlj}(r)}{r} \right]^2 \quad (4.14c)$$

are listed in Table IV for $r = 10.0, 11.5, 13.5,$ and 15.0 fm. It is seen that for these large values of r the inequality (4.13c) is indeed fulfilled.

The calculated values of $\bar{\rho}_{nlj}(r)$ can be compared with those measured from sub-Coulomb pickup reactions.^{30–33} However, it should be noted that these experiments actually measure the quantity $S_{nlj} \bar{\rho}_{nlj}(r)$, where S_{nlj} is the spectroscopic factor for the corresponding single-particle state in ²⁰⁷Pb.

The spectroscopic factor is given by the following expression,⁴¹

$$S_{nlj} = \int \bar{u}_{nlj}^2(r) [m/\bar{m}(r; E_{nlj})] dr. \quad (4.15)$$

These calculated spectroscopic factors are listed in Table V. They can be identified with the so-called ‘‘absolute’’ spectroscopic factors.⁴⁴ They cannot be compared readily with measured values because the latter do not include the admixture of the single-particle wave function in highly excited states of ²⁰⁷Pb, since these admixtures are hardly accessible to experiment. For completeness, Table V also gives the spectroscopic factors of particle states.

Table IV shows that the calculated asymptotic densities $S_{nlj} \bar{\rho}_{nlj}(r)$ are in excellent agreement with the experimental values. We note that this agreement would not have been as satisfactory if we had not introduced the effects associated with the Perey damping factor and with the spectroscopic factor. The sum

$$(S\bar{\rho})_{\text{tot}}(r) = \sum_{\text{occ}} S_{nlj} \bar{\rho}_{nlj}(r) \quad (4.16)$$

is represented by the solid curve in Fig. 11. The points represent the experimental total neutron density,^{31,33} which is found by summing the experimental values from Table IV. It is seen that excellent agreement exists between the calculated and measured values. This agreement is better than that obtained from the best mean field approaches.⁴³ We note that in the latter the spectroscopic factors are set equal to unity; Table IV shows that this would somewhat spoil the agreement between our model and experiment. In Fig. 11 the dashed curve represents the quantity $(S\bar{\rho})_{\text{tot}}(r)$ in the Hartree-Fock approximation. It is seen to decrease too rapidly with increasing r ; this reflects the fact that the hole states are overbound in the Hartree-Fock approximation.

D. Occupation probabilities

The dispersion integral on the right-hand side of Eq. (1.5) can be divided into two parts, one of which arises from the integration over E' from E_F to $+\infty$ and the other from an integration from $-\infty$ to E_F . We adopt a notation similar to that in Ref. 41 and write

$$\Delta\mathcal{V}(r; E) = \Delta\mathcal{V}_{\text{PO}}(r; E) + \Delta\mathcal{V}_{\text{CO}}(r; E), \quad (4.17)$$

$$\Delta\mathcal{V}_{\text{PO}}(r; E) = \frac{P}{\pi} \int_{E_F}^{\infty} \frac{\mathcal{W}(r; E')}{E' - E} dE', \quad (4.18a)$$

$$\Delta\mathcal{V}_{\text{CO}}(r; E) = \frac{P}{\pi} \int_{-\infty}^{E_F} \frac{\mathcal{W}(r; E')}{E' - E} dE'. \quad (4.18b)$$

Actually, the quantities $\Delta\mathcal{V}_{\text{PO}}$ and $\Delta\mathcal{V}_{\text{CO}}$ diverge in our present model, but this is of no importance in the present context because one can use the subtracted dispersion relations.¹⁵ Correspondingly, the E mass \bar{m} can be written in the following form,⁴¹

$$\frac{\bar{m}(r; E)}{m} = \frac{\bar{m}_{\text{PO}}(r; E)}{m} + \frac{\bar{m}_{\text{CO}}(r; E)}{m} - 1. \quad (4.19)$$

Note that in the frame of our assumption of symmetry (2.13), \bar{m}_{CO} is the reflection of \bar{m}_{PO} about E_F :

TABLE IV. Single particle densities at distance r .

nlj		$r = 10.0$ fm (10^{-5} n/fm ³)	$r = 11.5$ fm (10^{-6} n/fm ³)	$r = 13.5$ fm (10^{-7} n/fm ³)	$r = 15.0$ fm (10^{-8} n/fm ³)
$3p_{1/2}$	ρ	3.12	3.76	2.34	3.01
	$\bar{\rho}$	3.98	4.83	3.00	3.86
	$S\bar{\rho}$	3.17	3.84	2.39	3.07
	Expt. ^a	3.53	4.45	2.89	3.84
	Expt. ^b	3.84			4.11
$3p_{3/2}$	ρ	5.31	5.94	3.33	3.97
	$\bar{\rho}$	6.83	7.67	4.31	5.14
	$S\bar{\rho}$	5.56	6.25	3.51	4.18
	Expt. ^a	5.48	6.20	3.50	4.19
	Expt. ^b	6.14			4.67
$2f_{5/2}$	ρ	4.35	4.07	1.91	2.05
	$\bar{\rho}$	5.66	5.33	2.50	2.68
	$S\bar{\rho}$	4.56	4.30	2.02	2.16
	Expt. ^a	4.33	4.28	2.13	2.37
	Expt. ^b	4.53			2.44
$2f_{7/2}$	ρ	3.72	2.79	0.97	0.83
	$\bar{\rho}$	4.90	3.70	1.29	1.10
	$S\bar{\rho}$	4.17	3.15	1.10	0.94
	Expt. ^a	3.63	2.98	1.16	1.08
	Expt. ^b	3.46			1.01
$1i_{13/2}$	ρ	2.34	1.33	0.36	0.28
	$\bar{\rho}$	3.08	1.76	0.48	0.37
	$S\bar{\rho}$	2.49	1.42	0.39	0.30
	Expt. ^a	2.28	1.29	0.35	0.26
	Expt. ^b	2.01			0.23
$1h_{9/2}$	ρ	1.07	0.61	0.16	0.11
	$\bar{\rho}$	1.46	0.83	0.22	0.16
	$S\bar{\rho}$	1.24	0.71	0.19	0.13
	Expt. ^c	1.13	0.63	0.16	0.11
	Expt. ^d	0.86			
Total	ρ	19.9	18.5	9.1	10.3
	$\bar{\rho}$	25.9	24.1	11.8	13.3
	$S\bar{\rho}$	21.2	19.7	9.6	10.8
	Expt. ^{a,c}	20.4	19.8	10.2	11.9
	Expt. ^{b,d}	20.8			

^aExperimental densities from Ref. 31.

^bExperimental densities from Ref. 32 (quoted in Ref. 33 for $r = 10$ fm).

^cEstimated, not measured, from Ref. 31.

^dExperimental density from Ref. 33.

$$\bar{m}_{pO}(r; E + E_F) = \bar{m}_{cO}(r; E_F - E) . \quad (4.20)$$

Algebraic expressions of \bar{m}_{pO} and \bar{m}_{cO} can be obtained from Eq. (3.21) of Ref. 15.

The occupation probability of the single-particle state (n, l, j) is approximately given⁴¹ in the case of a hole state ($E_{nlj} < E_F$) by

$$N_{nlj} = \int_0^\infty \bar{u}_{nlj}^2(r) [2 - \bar{m}_{pO}(r; E_{nlj})/m] dr , \quad (4.21a)$$

and in the case of a particle state ($E_{nlj} > E_F$) by

$$N_{nlj} = \int_0^\infty \bar{u}_{nlj}^2(r) [\bar{m}_{cO}(r; E_{nlj})/m - 1] dr . \quad (4.21b)$$

The calculated occupation probabilities are listed in

Table V. We note that the calculated total number of neutrons in the valence orbits is equal to 45.2. It differs from 44 because the repletion of the valence shell above the Fermi energy in part derives from the depletion of deeply bound orbits; conversely, the depletion of the valence shell below the Fermi energy in part feeds orbits which lie in the continuum, i.e., at positive energy.

Interest in occupation probabilities has been renewed by the recent measurements⁴⁵ for the $3s_{1/2}$ proton shell in ²⁰⁸Pb. Only small differences should be expected between the occupation probabilities of proton and neutron single-particle states.⁴¹ Hence, it is of interest to note that the value $N_{3p_{1/2}}^{(n)} = 0.86$ calculated here is close to the experimental result $N_{3s_{1/2}}^{(p)} = 0.82 \pm 0.09$ quoted in

TABLE V. Spectroscopic factors, occupation numbers, and rms radii of valence neutron particle and hole states in ²⁰⁸Pb.

nlj	S_{nlj}	N_{nlj}	R_{nlj}^{rms} (fm)
$3d_{3/2}$	0.90	0.07	8.02
$2g_{7/2}$	0.86	0.10	7.15
$4s_{1/2}$	0.91	0.06	8.47
$3d_{5/2}$	0.88	0.08	7.62
$1j_{15/2}$	0.82	0.13	6.73
$1i_{11/2}$	0.82	0.12	6.53
$2g_{9/2}$	0.81	0.12	6.70
$3p_{1/2}$	0.80	0.86	6.36
$2f_{5/2}$	0.81	0.87	6.18
$3p_{3/2}$	0.81	0.87	6.23
$1i_{13/2}$	0.81	0.87	6.36
$2f_{7/2}$	0.85	0.90	5.97
$1h_{9/2}$	0.85	0.90	5.93

Ref. 45. In addition, it has been found⁴⁶ that the ground state magnetization densities in ²⁰⁷Pb are quenched relative to predictions of the independent-particle model. This quenching has been attributed⁴⁶ to the partial occupancy of the neutron orbits.

E. rms radii of valence orbits

The rms radius for each nlj is calculated using the wave function $\bar{u}_{nlj}(r)$,

$$R_{nlj}^{\text{rms}} = \left[\int_0^\infty \bar{u}_{nlj}^2(r) r^2 dr \right]^{1/2}. \quad (4.22)$$

These are listed in Table V. From an average over the hole states, weighted by $2j+1$, we find an excess-neutron radius of 6.17 fm, in close agreement with the 6.21-fm radius deduced⁴³ in the mean field approach.

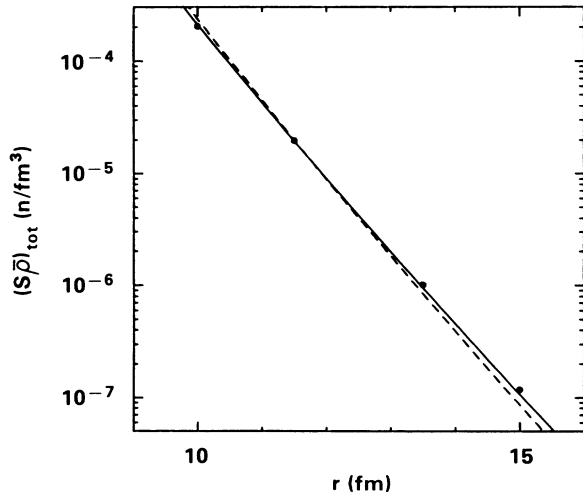


FIG. 11. Radial dependence of the quantity $(S\bar{\rho})_{\text{tot}}$. The points represent the experimental values and the solid line is calculated using the full mean field. The dashed line is calculated using the Hartree-Fock approximation with all spectroscopic factors set equal to unity.

Our values for each nlj cannot be compared exactly with those from Refs. 30–33 because the latter were deduced from the observed $S_{nlj}\bar{\rho}_{nlj}(r)$ using wave functions calculated with a local potential with an assumed spectroscopic factor, usually $S=1$. As a consequence, the values deduced here are larger than those quoted in Refs. 30–33. The differences are related in part to the asymptotic wave functions and to the related inequalities, i.e., (4.13a) and (4.13c), which are generated by the Perey damping factor. For the hole states and for the particle states with high spin values the differences are about 0.2 fm. However, for most particle states the differences are relatively large; in particular, the difference from Ref. 32 for the $4s_{1/2}$ orbit is 0.8 fm.

V. ENERGY DEPENDENCE OF THE RADIAL SHAPE OF $\mathcal{V}(r;E)$

A. Introduction

According to Eq. (1.4), the full potential $\mathcal{V}(r;E)$ is the sum of the Hartree-Fock potential $\mathcal{V}_H(r;E)$ and of the dispersive contribution $\Delta\mathcal{V}(r;E)$. The potential $\mathcal{V}_H(r;E)$ has a Woods-Saxon shape whose geometrical parameters have been assumed to be independent of energy, see Eqs. (3.1) and (3.3). In contrast, the radial shape of $\Delta\mathcal{V}(r;E)$ depends on energy because the ratio $[\Delta V_v(E)/\Delta V_s(E)]$ of the strengths of its volume and surface-peaked components depends upon energy. In subsections B, C, and D we discuss, respectively, the radial dependence of $\Delta\mathcal{V}(r;E)$, the radial dependence of the full potential $\mathcal{V}(r;E)$, and the energy dependence of the volume integral of $\mathcal{V}(r;E)$.

B. Radial shape of $\Delta\mathcal{V}(r;E)$

Because of the symmetry assumption, Eq. (2.13), the dispersive contribution $\Delta\mathcal{V}(r;E)$ is skew-symmetric with respect to E_F :

$$\Delta\mathcal{V}(r;E + E_F) = -\Delta\mathcal{V}(r;E_F - E). \quad (5.1)$$

The quantity $\Delta\mathcal{V}(r;E)$ is the sum of a volume component $\Delta\mathcal{V}_v(r;E)$ with the Woods-Saxon geometry $f(X_H)$ and of a surface component $\Delta\mathcal{V}_s(r;E)$ whose radial shape is given by the derivative of the Woods-Saxon geometry $f(X_s)$, see Eq. (2.18). From the geometry parameters and the dispersive strengths, we calculate the various potentials; they are plotted in Figs. 12(a), 12(b), and 12(c) for $E=0, 5$, and 24 MeV, respectively. These results are in semiquantitative agreement with those obtained in Ref. 5 from a cruder model.

C. Radial shape of $\mathcal{V}(r;E)$

Equations (1.4) and (2.21)–(2.23) yield

$$\mathcal{V}(r;E) = V_v(E)f(X_H) + \Delta\mathcal{V}_s(r;E). \quad (5.2)$$

Since the surface-peaked contribution is not very narrow and since its strength is not large, the full potential has a radial shape which closely resembles a Woods-Saxon potential. This is exhibited in Fig. 13 for neutron energies of 5 and 24 MeV. For each energy the solid curve

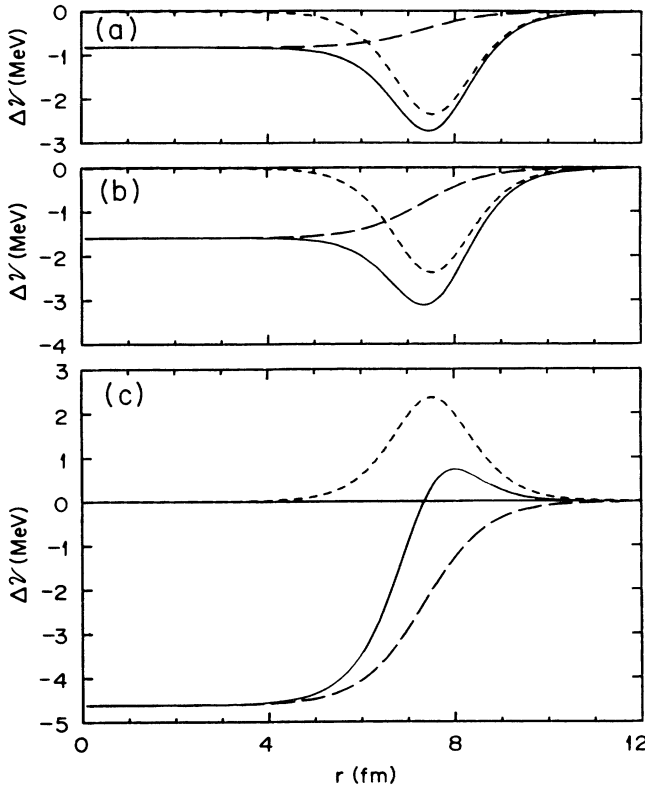


FIG. 12. The solid curves represent the dispersive contribution $\Delta\mathcal{V}(r;E)$ for (a) $E=0$ MeV, (b) 5 MeV, and (c) 24 MeV. The long-dashed and short-dashed lines give the volume and surface components, $\Delta\mathcal{V}_v$ and $\Delta\mathcal{V}_s$, respectively.

represents $\mathcal{V}(r;E)$ and the dashed curve the corresponding “effective” Woods-Saxon potential $\mathcal{V}_e(r;E)$, with a depth equal to $V_v(E)$ [solid curve in Fig. 2(b)], a diffuseness equal to a_H , and a radius R_v which is determined by the requirement that the volume integrals of $\mathcal{V}_e(r;E)$ and $\mathcal{V}(r;E)$ are equal. We recall that the volume integral per nucleon of a Woods-Saxon potential

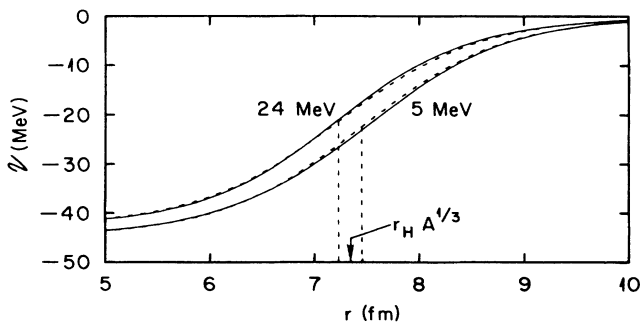


FIG. 13. The solid curves give the full potential $\mathcal{V}(r;E)$ for $E=5$ and 24 MeV. The dashed lines represent an “effective” Woods-Saxon potential $\mathcal{V}_e(r;E)$ with the same depth, diffuseness, and volume integral as for $\mathcal{V}(r;E)$. The vertical dashed lines represent the radii for the two Woods-Saxon potentials, and the arrow shows the Hartree-Fock radius.

with depth V , diffuseness a , and radius $R=rA^{1/3}$ is given approximately by

$$J/A = -\frac{4\pi}{3} V r^3 [1 + (\pi a/R)^2]. \quad (5.3)$$

The vertical dashed lines in Fig. 13 indicate the radii R_v for the plotted “effective” Woods-Saxon potentials and the arrow indicates the Hartree-Fock radius.

The radius parameter r_v of this “effective” Woods-Saxon potential depends on energy. This dependence is represented by the solid curve in Fig. 14. The behavior of $r_v(E)$ can be understood by comparison with the similar curve for $\Delta V_s(E)$ in Fig. 3(b). By adding a surface peaked contribution $\Delta\mathcal{V}_s(r;E)$ to the model Woods-Saxon volume potential $V_v(E)f(X_H)$, one indeed obtains an “effective” Woods-Saxon potential whose radius is larger than R_H if ΔV_s is attractive and smaller than R_H if ΔV_s is repulsive.⁶ We see from Fig. 3 that ΔV_s changes sign at the Fermi energy and again at $E=11.6$ MeV. At those energies the effective radius r_v is identical to the radius of the Hartree-Fock potential.

The property that the calculated radius decreases for energies larger than 4 MeV is consistent with empirical evidence;⁴ in Fig. 14 the dashed curves show the empirical variation as deduced in Ref. 4 from a purely phenomenological optical model analysis. We note that the radius of the effective Woods-Saxon potential decreases with decreasing E in the energy domain $[-10$ MeV, 0] which corresponds to the two valence shells. This is in keeping with the results recently obtained from a related but different approach.^{47,48}

D. Volume integral

It is customary to characterize the strength of an average potential by its volume integral per nucleon. This quantity is shown in Fig. 15. It is seen that the solid circles are compatible with a linear energy approximation (E in MeV),

$$J_{\mathcal{V}}/A \approx (-412 + 2.6E) \text{ MeV fm}^3 \quad \text{for } 4 < E < 40 \text{ MeV}. \quad (5.4)$$

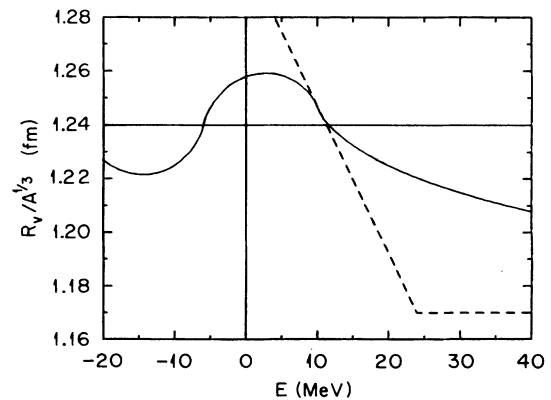


FIG. 14. Energy dependence of the radius parameter $r_v = R_v/A^{1/3}$ Eq. (1.3c), of the “effective” Woods-Saxon potential (dashed lines in Fig. 13). The dashed curve is the empirical radius from Ref. 4.

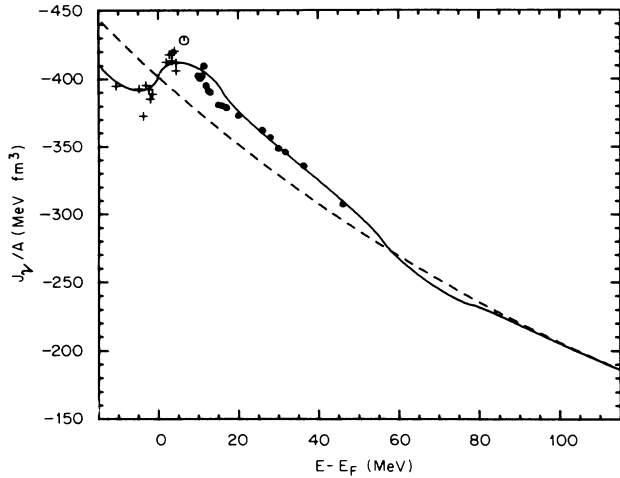


FIG. 15. Volume integrals for the Hartree-Fock potential and for the full potential. The Hartree-Fock curve (dashed) is calculated using the dashed curve in Fig. 1(a). The full potential curve (solid) is calculated using the sum of the surface and the volume terms [dashed curve in Fig. 1(c) and solid curve in Fig. 1(a)]. Each symbol represents the sum of the surface term for the corresponding symbol in Fig. 3(b) plus the volume term deduced from the solid curve in Fig. 2(b).

This approximation is representative of parametric forms previously proposed within the framework of purely phenomenological analyses; see, e.g., Ref. 49. Hence the typical low-energy dependence implied by the DR usually cannot be empirically exhibited if one limits oneself to positive energies and to the volume integrals.^{50,51} Figure 15 shows, however, that the volume integral at negative energy strongly deviates from the extrapolation of the linear approximation (5.4). This extrapolation would greatly overbind the valence single-particle states and would yield valence single-particle wave functions whose asymptotic values at large distance would be very different from those found from the analysis of sub-Coulomb pickup experiments (Sec. IV C). We note that the typical energy dependence of J_V at negative energy mainly reflects the energy dependence of the surface-peaked contribution (Fig. 3) or, equivalently, of the radius of the “effective” Woods-Saxon potential (Fig. 14).

VI. ENERGY-DEPENDENT SURFACE GEOMETRY FOR $E < 10$ MeV

A. Introduction

Although the model investigated in Secs. III–V involves very few adjustable constants, it is remarkably successful in describing a large body of experimental data in a broad energy domain $-20 < E < 165$ MeV. This success results from the use of the DR. One should not expect this simple model to describe the data in complete detail in the whole energy domain. Indeed, the DR approach describes only the average effect of the couplings between the single-particle states and the core excitations. Some couplings to specific core excitations

may introduce corrections to the Hartree-Fock field which (i) vary rapidly with energy, and (ii) depend on the angular momentum and parity of the single-particle state. Examples are shown in Figs. 4.45a and 4.49 of Ref. 14.

Such specific effects should probably best be taken into account explicitly rather than in the framework of the standard optical model. Nevertheless, one may wonder whether weaknesses of the simple model of Secs. III–V in the low energy domain ($4 \leq E \leq 11$ MeV) could not be cured by appropriate refinements. We focus on low energies because the simple model predicts too large total cross sections for $7 < E < 11$ MeV (Fig. 7), while for $5.5 \leq E \leq 9$ MeV it yields poor agreement with the measured differential cross sections at scattering angles larger than 100° (Fig. 6). This suggests that our simple parametrization of $\mathcal{W}_s(r; E)$ may not be fully adequate at these low energies. In the present section we discuss a model in which the geometrical parameters of $\mathcal{W}_s(r; E)$ depend upon energy for $E < 10$ MeV, in contrast to the model used in Secs. III–V. In Sec. VII we shall investigate a model in which $\mathcal{W}_s(r; E)$ depends on the nucleon orbital angular momentum.

B. Fitting with an energy-dependent surface geometry

Purely phenomenological optical-model fits⁴ of the differential cross sections suggest that a_s tends to decrease and r_s to increase with decreasing E for $4 < E < 10$ MeV. In the present section we shall retain the radial shape of $\mathcal{W}_s(r; E)$ given by Eq. (2.10), but let a_s and r_s depend on E . The geometrical parameters of the volume contribution are kept the same as in Secs. II–V; see Eqs. (3.1)–(3.3). We introduce a surface-peaked real contribution

$$\Delta \mathcal{V}_s(r; E) = -4a_d \Delta V_s(E) \frac{d}{dr} f(X_d). \quad (6.1)$$

In principle, this equation introduces two more parameters, a_d and r_d . However, since preliminary searches showed that meaningful fits could not be made for so many parameters, we allow $a_d(E)$ to differ from $a_s(E)$ but require

$$r_d(E) = r_s(E). \quad (6.2)$$

The preliminary searches showed this to be a good approximation.

We thus perform least squares fits to the ten angular distributions for $4 \leq E \leq 11$ MeV with the following six adjustable parameters: V_v , W_s , ΔV_s , a_s , r_s , and a_d . In Fig. 16 the solid points represent the resulting V_v ; the open circles show the V_H deduced, as in Fig. 2, by subtraction of the dispersion correction $\Delta V_v(E)$. The curves are reproduced from Fig. 2. The points fall somewhat below the solid curve but support the DR prediction that $V_v(E)$ is nearly independent of energy for $4 \leq E \leq 11$ MeV. Following a procedure analogous to that used in Sec. III D, we search again with V_v fixed on the solid curve. The resulting geometrical parameters r_s , a_s , and a_d are shown in Fig. 17. The values of a_s tend

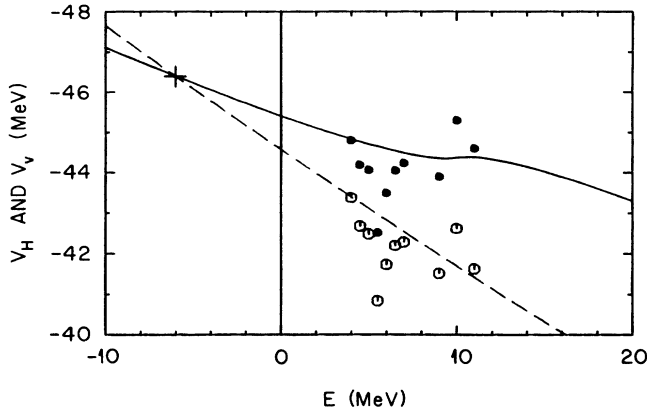


FIG. 16. Potential depths for the model with energy dependent radius and diffuseness of the surface imaginary potential (Sec. VI). The solid symbols represent the empirical values of V_v determined by least-squares fits to the data, and the open symbols represent V_H deduced by subtraction of the DR volume correction represented by the dashed curve in Fig. 2(a). The curves and the cross are from Fig. 2(b).

to decrease and those of r_s to increase with decreasing E for $4 < E < 10$ MeV, as expected from purely phenomenological analyses, as mentioned above.

The radial shape of $\Delta\mathcal{V}_s(r;E)$ cannot easily be calculated from the DR, Eq. (2.16a), since the geometrical parameters r_s and a_s depend on energy. Moreover, the fluctuations of the diffuseness a_d reflect the property that

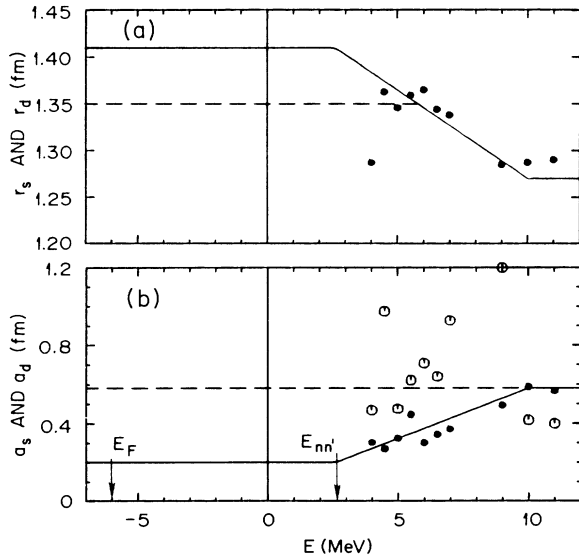


FIG. 17. Energy dependent geometries for the model in Sec. VI. The solid symbols represent the empirical radius r_s and diffuseness a_s of the surface imaginary potential, and the open symbols represent the empirical diffuseness a_d of the real surface potential. The solid lines are visual fits to the solid symbols. Below the lowest inelastic threshold, which is indicated by the arrow at $E_{nn'} = 2.6$ MeV, r_s and a_s are assumed to be constant. The dashed lines represent the assumed values of r_d and a_d for the model, as discussed in the text.

the fits mainly determine the volume integral of $\Delta\mathcal{V}_s$, which is proportional to $a_d\Delta\mathcal{V}_s$. Accordingly, we apply the DR in terms of volume integrals, for which it reads

$$J_{\Delta\mathcal{V}_s} = \frac{P}{\pi} \int_{-\infty}^{+\infty} \frac{J_{\mathcal{W}_s}(E')dE'}{E' - E}. \quad (6.3)$$

In Fig. 18 the volume integrals for the empirical $\Delta\mathcal{V}_s$ and \mathcal{W}_s are represented by solid symbols, while the curves are reproduced from Fig. 3, each multiplied by 8.1 fm^3 to approximately convert from well depth to volume integral per nucleon. A comparison between Figs. 3 and 18 shows that the volume integrals for the imaginary part are about the same for the two models, but that the present energy-dependent geometry yields better agreement with the DR predictions of the real surface term for $4 \leq E \leq 11$ MeV.

C. Extrapolation to negative energies

As in Sec. IV, we wish to extrapolate the real surface term to negative energies. In the present case the extrapolation is uncertain because the energy dependence of the geometrical parameters is unknown for $E < 4$ MeV. We therefore make the following simplifications. We approximate the energy dependences of r_s and a_s in the experimental energy region by the straight line segments

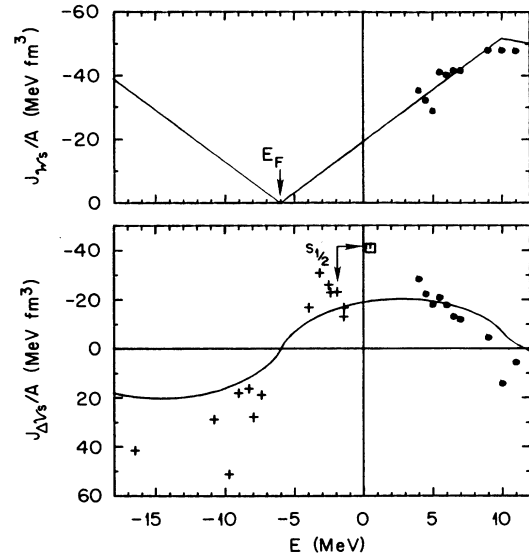


FIG. 18. Energy dependence of the volume integrals per nucleon of the surface-peaked components of the imaginary and real parts of the optical model potential for the same searches as in Fig. 17. The curves are from Fig. 3 with a renormalization factor of 8.1 fm^3 . The dots represent empirical values obtained with V_v defined by the solid curve in Fig. 16. The crosses represent the real surface volume integrals required to reproduce experimental bound state energies. The open symbol shows the volume integral required to reproduce the s -wave potential scattering in the 0.05- to 1-MeV region. The arrows show the relation to the $4s_{1/2}$ particle state. For both the crosses and the open symbol, the surface geometries shown by curves in Fig. 17 have been used.

shown by solid curves in Fig. 17, and we extrapolate to negative energies assuming that both r_s and a_s remain constant below the inelastic threshold at 2.6 MeV. The solid curves for $r_s(E)$ and $a_s(E)$ represent the following expressions (in fm):

$$r_s = 1.41 \quad \text{and} \quad a_s = 0.2 \quad \text{for} \quad E < 2.6 \text{ MeV}, \quad (6.4a)$$

$$r_s(E) = 1.41 - 0.0189(E - 2.6) \quad \text{for} \quad 2.6 < E < 10 \text{ MeV}, \quad (6.4b)$$

$$a_s(E) = 0.2 + 0.0513(E - 2.6) \quad \text{for} \quad 2.6 < E < 10 \text{ MeV}, \quad (6.4c)$$

and

$$a_s = 0.58 \quad \text{and} \quad r_s = 1.27 \quad \text{for} \quad E > 10 \text{ MeV}.$$

To predict the corresponding real geometry from the DR would require a numerical evaluation of the dispersion integral in Eq. (2.16a). Here we use a simplified approach. We assume $r_d = 1.35$ fm for $E < 5.8$ MeV, as indicated by the dashed curve in Fig. 17(a), and a constant diffuseness $a_d = 0.58$ fm, as shown by the dashed curve in Fig. 17(b).

For this model the crosses in Fig. 18(b) represent the volume integrals required to bind each particle and hole state at its experimental energy. A comparison of Figs. 3(b) and 18(b) indicates that the required $|\Delta V_s|$ for the present model show poor agreement with the DR curve; they are generally larger than the DR predictions. This poor agreement results from the increase of the radius parameter for $\Delta V_s(r; E)$ from 1.27 to 1.35 fm. Furthermore, the predicted spreading width of the $1h_{11/2}$ state is only 2 MeV, in poor agreement with the experimental width.

D. Discussion

Column 3 of Table II lists the χ^2/N deduced by comparing the experimental angular distributions with predictions from this model, as defined by the curves shown in Figs. 16–18. Relative to the fixed geometry model (column 2) these show about a factor of 2 improvement for energies of 5, 6, 6.5, and 7 MeV, but little change for $E = 4.5, 5.5, 10,$ and 11 MeV. The fact that χ^2/N is worse at 4 MeV is a consequence of the poor description given by the model for the empirical r_s at 4 MeV [see Fig. 17(a)].

We find several objections to the model discussed in the present section. (i) The complications introduced by considering energy-dependent empirical functions $r_s(E)$ and $a_s(E)$ did not lead to a significant improvement between the fitted values and the DR predictions. (ii) The empirical V_v scatter from one energy to the next. (iii) The large imaginary radius parameter r_s implies that at negative energies the peak for the real surface term lies well outside the Hartree-Fock radius. This means that the surface strength $|\Delta V_s|$ must be increased beyond the DR predictions in order to fit the experimental binding energies, particularly those for the hole states and for the particle states with large l values. Furthermore,

the predicted width of the $1h_{11/2}$ hole state is too small because the radius of the imaginary surface potential is too large to allow good overlap with the $1h_{11/2}$ wave function.

VII. ANGULAR-MOMENTUM-DEPENDENT MODEL

A. Introduction

In the models studied above it was assumed that the mean field is independent of the orbital angular momentum l of the incident neutron. The effect of a possible l dependence would be especially important at low energies because the number of partial waves is limited by the centrifugal barrier. Figure 19 shows the contribution of each partial wave to the angle-integrated cross sections predicted by the fixed geometry model of Secs. III–V, for $E < 12$ MeV. At 7 MeV, for example, the total cross section arises mainly from partial waves with $l = 0$ to 6. One cannot deduce $\mathcal{W}(r; E)$ separately for each partial wave; therefore, we introduce a limited l dependence by splitting $W_s(E)$ into two empirical functions of energy, $W_{bs}(E)$ and $W_{cs}(E)$. Here, the subscripts b and c denote the groups of partial waves which are represented in Fig. 19 by the dashed and solid curves, respectively. Group b contains $l = 1, 3,$ and $6,$ and group c the remainder. As we show below, this particular grouping of partial waves leads to consistency with the DR and good fits to the scattering data. From comparisons with the fits achieved with several other groupings, including a parity dependence, we concluded that the present grouping is probably the best choice that can be made, under the restriction that there be only two groups.

The DR introduces a corresponding l dependence for the real surface potential. For the initial phenomenological analyses without the DR constraint, our model for this section will have seven free parameters, namely

$$W_{bs} \quad \text{and} \quad \Delta V_{bs} \quad \text{for group } b \quad (l = 1, 3, \text{ or } 6), \quad (7.1a)$$

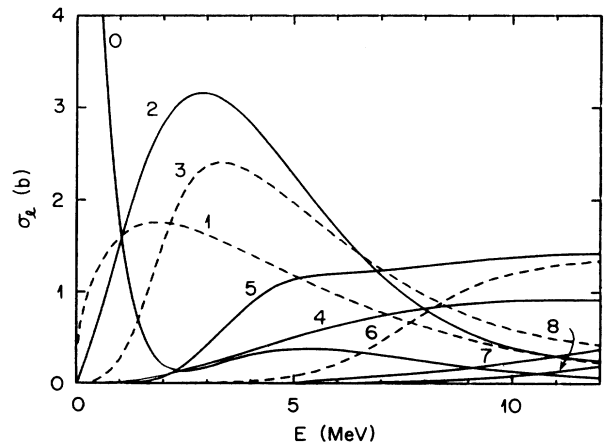


FIG. 19. Partial wave total cross sections for the fixed geometry model from Sec. III. The dashed and solid lines denote, respectively, the partial wave groups b and c introduced in Sec. VII.

W_{cs} and ΔV_{cs} for group c (other l values), (7.1b)

along with V_v , a_s , and a_d . The remaining parameters r_H , a_H , and r_s will be held fixed as in Eqs. (3.1)–(3.3). We emphasize that, in contrast to the model of Sec. VI, the radius parameter r_s is assumed to be constant.

B. Analysis of the cross sections for $4 < E < 11$ MeV

Least-squares fits to the experimental cross sections with these seven adjustable parameters yield excellent fits, as well as χ^2 minima that are surprisingly well defined for so many parameters. In Fig. 20 the solid symbols show V_v and the open symbols represent the quantity V_H deduced by subtraction of $\Delta V_v(E)$, as was done in Fig. 2. These symbols are in excellent agreement with the smooth curves for $V_v(E)$ and $V_H(E)$, which have been reproduced from Fig. 2.

As in the preceding models, Secs. III–VI, we now fix V_v on the solid curve and repeat the fits. The resulting values of a_s and a_d are shown in Fig. 21. The symbols for the real diffuseness parameter a_d show considerable scatter; this is indicative, as in Sec. VI, of the fact that the cross section mainly depends upon the product $a_d \Delta \mathcal{V}_s$. The volume integrals of the empirical $\Delta \mathcal{V}_s$ and \mathcal{W}_s are shown in Figs. 22(a) and 22(b), respectively, with solid points for group b and open circles for c . We note that the imaginary integral for group b lies systematically above that for group c . In both cases the volume integrals are well approximated by the following LS parametrizations:

$$J_{\gamma \mathcal{W}_s}(E)/A = 0 \quad \text{for } -6 < E < -2 \text{ MeV}, \quad (7.2a)$$

$$J_{\gamma \mathcal{W}_s}(E)/A = -6.44(E + 2) \quad \text{for } -2 < E < 6.5 \text{ MeV}, \quad (7.2b)$$

$$J_{\gamma \mathcal{W}_s}(E)/A = -0.835(72 - E) \quad \text{for } 6.5 < E < 72 \text{ MeV}. \quad (7.2c)$$

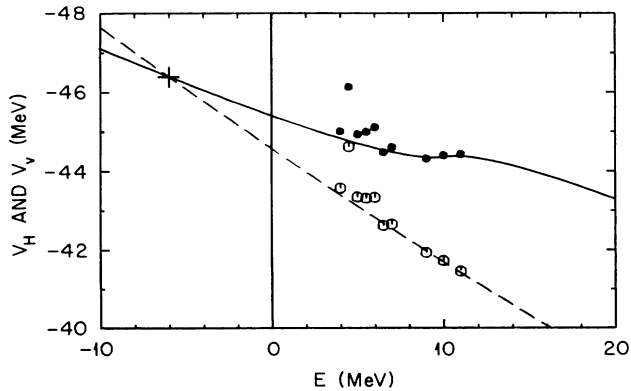


FIG. 20. The volume depths determined with the model for which W_i depends on orbital angular momentum. The solid symbols represent empirical values of V_v determined by least-squares fits to the data and the open symbols represent V_H deduced by subtraction of the volume correction as represented by the dashed curve in Fig. 2(a). The curves and the cross are from Fig. 2(b).

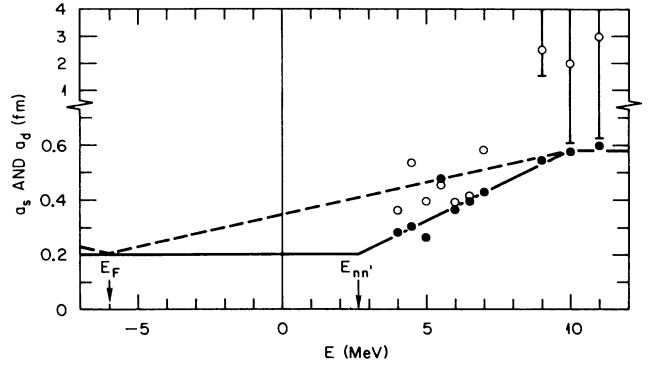


FIG. 21. Surface diffuseness parameters for the angular-momentum-dependent model. The solid and open symbols denote the empirical a_s and a_d , respectively, from the same searches as in Fig. 20. The solid curve for a_s is the same curve as in Fig. 17. The dashed line is an approximation to a_d . The vertical arrow at 2.6 MeV points to the lowest inelastic threshold.

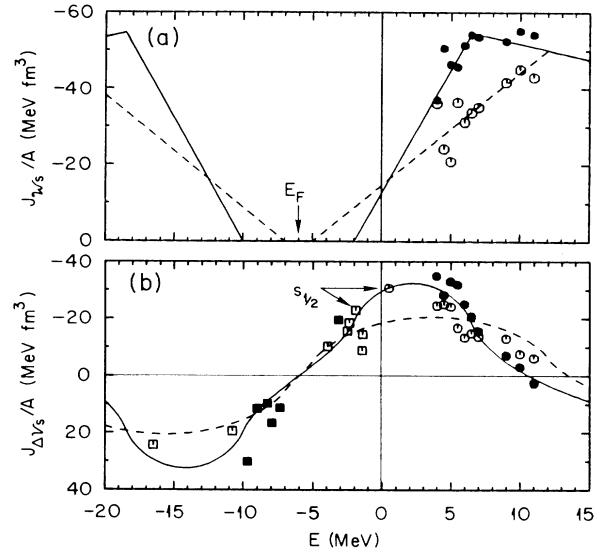


FIG. 22. Energy dependence of the volume integrals per nucleon of the surface-peaked components of the imaginary and real parts of the angular-momentum-dependent optical model potential. The solid dots and open circles represent empirical values for groups b ($l = 1, 3, 6$) and c ($l \neq 1, 3, 6$), respectively, obtained by searches with V_v fixed by the solid curve in Fig. 20. The square symbols represent the volume integrals required to reproduce the experimental bound state energies using the surface geometries given by the curves in Fig. 21. These are also shown solid and open for the orbital angular momentum of groups b and c , respectively. The open circle at 0.5 MeV is for s -wave scattering, as in Fig. 18, and the connecting arrow indicates the $4s_{1/2}$ particle state. The lines in (a) represent visual LS parametrizations and the curves in (b) are the corresponding DR predictions; these are solid for group b and dashed for group c .

for group *b* [solid lines in Fig. 22(a)], and

$$J_{\mathcal{W}_s}(E)/A = 0 \quad \text{for } -6 < E < -5 \text{ MeV}, \quad (7.3a)$$

$$J_{\mathcal{W}_s}(E)/A = -2.95(E+5) \quad \text{for } -5 < E < 12 \text{ MeV}, \quad (7.3b)$$

$$J_{\mathcal{W}_s}(E)/A = -0.835(72-E) \quad \text{for } 12 < E < 72 \text{ MeV}. \quad (7.3c)$$

for group *c* [dashed lines in Fig. 22(a)]. In both cases the volume integral is set equal to zero for $E > 72$ MeV. Note that the decreasing line segments above the maxima [Eqs. (7.2c) and (7.3c)] are assumed to be the same as for the fixed geometry model of Fig. 3.

From these LS parametrizations and from the DR, Eq. (6.3), we calculate the real surface volume integrals that are represented in Fig. 22(b) by solid and dashed curves for *b* and *c*, respectively. These predictions agree well with the points. In particular, it is noticeable that the DR correctly predicts the crossover near 7 MeV, with the solid points being above the open symbols for $E < 7$ MeV but below for $E > 7$ MeV.

C. Cross sections for the angular momentum dependent model

A calculation of the cross section requires a complete parametrization of $\mathcal{W}_s(r;E)$ and $\Delta\mathcal{V}_s(r;E)$. That is, it requires not only the radius r_s and the volume integrals, but also the surface diffuseness parameters. In Fig. 21 the solid curve, which is redrawn from Fig. 17(b), gives a good representation of a_s . To construct an approximate curve for $a_d(E)$, we integrate the DR in the form of Eq. (2.16) using the parametrization of the imaginary surface potential represented by the curves in Figs. 21 and 22(a). The results for $E < 9$ MeV are adequately described by the dashed curve in Fig. 21. This curve is consistent with the fitted values (open symbols) in that region. The fitted a_d for $E = 9, 10, \text{ and } 11$ MeV lie well above the curve, but this is not very meaningful because in this energy domain the volume integral $J_{\Delta\mathcal{V}_s}$ is quite small, so that the empirical value of a_d is quite uncertain. For the sake of simplicity, we will use the curve for $a_d(E)$ and justify this approximation by noting that the effect of the real surface term is small for energies near its zero crossing. Thus, we take (in fm)

$$a_d(E) = 0.2 + 0.024(E - E_F) \quad \text{for } E < 10 \text{ MeV}, \quad (7.4a)$$

$$a_d(E) = 0.58 \quad \text{for } E > 10 \text{ MeV}. \quad (7.4b)$$

In Fig. 6 the solid curves show the differential cross sections predicted for $4 \leq E \leq 11$ MeV from this model with parameters represented by the curves in Figs. 20–22 and with the constant values for r_H , a_H , and r_s . The corresponding χ^2/N are listed in column 4 of Table II. The model is seen to describe the observed angular distributions significantly better than the preceding two models.

The predicted total cross sections are represented by solid lines in Figs. 7 and 8(a); comparisons to the dashed

curve for fixed geometry shows that the present model is an improvement for $7 < E < 12$ MeV. The predicted total cross sections average only 0.9% less than the values tabulated in Table I. For $E > 12$ MeV the two models are essentially identical.

D. Extrapolation to $E < 1$ MeV and negative energies

For this model we determine the surface strength ΔV_s required to reproduce the experimental single-particle energies. In these calculations the depth $V_v(E)$ is taken from the solid curve in Fig. 20 and the diffuseness a_d from the dashed line in Fig. 21 with the assumption of symmetry about E_F . The square symbols in Fig. 22 show the resulting real surface volume integrals for the particle and hole states. These symbols are shown solid for $l = 1, 3, \text{ and } 6$ and open for other orbits, in like manner to the symbols for $E > 0$. We see that the values of ΔV_s represented by the squares agree quite well with the DR prediction. This agreement is similar to that obtained with the fixed geometry model of Secs. III–V and is better than for the model of Sec. VI, in which r_s and r_d depend on energy. The arrows in Fig. 22(b) point to the values required for the $4s_{1/2}$ particle state and for the average *s*-wave scattering function^{19,20} for 0.5-MeV neutrons. The agreement of these two points is further evidence that the shell model and optical model join smoothly at zero energy.

E. Discussion

In the present section we allowed $\mathcal{W}_s(r;E)$ to be quite complicated for $E < 12$ MeV and to involve three smooth functions of energy. With this representation, we not only obtain good fits to the scattering distributions at low energies, but also determine empirical $\mathcal{V}(r;E)$ which are in close agreement with the DR predictions. We deliberately adopted an empirical point of view for this momentum-dependent model, and do not attempt a detailed theoretical justification. In fact, such an attempt would not be warranted because our analysis in terms of only two groups of partial waves is still an oversimplification. Nevertheless, we note that two quite different types of theoretical calculations^{52,53} suggest that particle-vibration couplings would give rise to an angular-momentum dependence of $\mathcal{W}_s(r;E)$. Additionally, experimental studies of neutron scattering on lead isotopes in the resonance region have exhibited doorway states in the *s*-, *p*-, and *d*-wave channels; these were interpreted as arising from particle-vibration couplings.^{20,54}

VIII. CONCLUSIONS

We have utilized the dispersion relationship (DR) between the imaginary and real potentials in an optical model analysis of a large body of data on $n + {}^{208}\text{Pb}$ for a broad energy domain. In our simplest model, Secs. III–V, the imaginary potential is characterized by geometrical parameters which are independent of energy; its energy dependence is entirely contained in the strengths of its volume and surface components, each of which is described by a smooth empirical function of en-

ergy. The corresponding real surface and volume components predicted by the DR are added to an empirical Hartree-Fock potential to yield the full real potential.

Our Hartree-Fock potential has a Woods-Saxon shape with fixed geometry and an exponential energy dependent depth. Thus, the intricate energy dependencies for the full real field are entirely defined by the DR. The radius of the real field has a characteristic energy dependence as the energy increases from -20 to $+20$ MeV (Fig. 14): it increases by about 3% when E increases from -12 MeV to 0, and decreases by about 2% from 5 to 15 MeV. These properties are consequences of the surface-peaked nature of the absorptive potential at low energies, and are therefore also expected to hold for other nuclei. The predicted depth of the real volume potential mainly decreases with increasing energy. However, in the domain from about 5 to 15 MeV it remains relatively constant (Fig. 2). This feature is a consequence of the property that the volume part of the absorptive potential becomes significant at energies larger than about 10 MeV; it is also expected to hold qualitatively for nuclei other than ^{208}Pb .

This simple model provides a good description of the data over a very broad energy domain which extends from -20 to 165 MeV. In particular, it predicts bound-state single-particle energies (Fig. 9) and wave functions (Fig. 11) which are in better agreement with experimental observations than can be found in any of the available microscopic calculations. It predicts the spreading width of the deep $1h_{11/2}$ hole state in excellent agreement with the observed width. Finally, it gives a very good description of the scattering distributions for $14 < E < 40$ MeV and provides an excellent description of the total cross section from 12 to 150 MeV.

The simple "fixed geometry" model investigated in Secs. III–V is quite successful. It is only in the limited energy domain from 5 to 12 MeV that it is not completely satisfactory. In this region the predicted total cross sections are too large and the differential cross sections do not fit the data well at large scattering angles. These failures probably reflect the inadequacies of our very simple imaginary potential in that region; the potential involves only one empirical function of energy for $E < 10$ MeV. We showed in Sec. VII that the discrepancies can be ameliorated by allowing the surface imaginary diffuseness to have an energy dependence and the surface imaginary strength to have two components, one for $l = 1, 3,$ and 6 and the other for the remaining partial waves. This more complicated model not only gives very good fits to the data, but also yields empirical values for the real parameters which are in better agreement with the DR predictions.

In conclusion, this work demonstrates that the DR can be used to deduce a mean nuclear field which is capable of describing a large body of experimental data over a large energy domain. In particular, it predicts remarkably well the shell model potential (at negative energy) from the extrapolation of the optical-model potential (at positive energy). This extrapolation is in good agreement with recent work^{47,48} which used a related but somewhat different approach.

ACKNOWLEDGMENTS

The authors wish to acknowledge fruitful and enlightening discussions with Dr. G. R. Satchler, Dr. R. Sartor, and Dr. R. D. Smith. We are also indebted to Dr. R. W. Finlay, Dr. S. M. Austin, Dr. R. L. Varner, and Dr. D. C. Larson for providing tabulated cross section data. Helpful comments by Dr. D. C. Larson and Dr. J. K. Dickens are appreciated. Oak Ridge National Laboratory is operated by Martin Marietta Energy Systems, Inc. for the U.S. Department of Energy under Contract No. DE-AC05-84OR21400. One of us (C.M.) acknowledges the hospitality and support of Oak Ridge National Laboratory and the Joint Institute for Heavy Ion Research during part of this work.

APPENDIX

Here, we evaluate experimental uncertainties in the total cross sections. The two sets of data^{19,20,27,28} represented by the points in Figs. 7 and 8(a) were both obtained by transmission measurements at the Oak Ridge Electron Linear Accelerator (ORELA); however, they were measured independently using different sources, flight paths, scatterers, and detectors. The plotted data represent energy averages of the measured cross sections. The data for Fig. 7 were obtained with particularly good energy resolution with a 200-m flight path. Averaging of such data in regions of strong resonance structure avoids errors of self-attenuation that can give cross sections that are too low when measured by transmission with poor energy resolution.

The total cross sections for $n + ^{208}\text{Pb}$ and $n + ^{\text{nat}}\text{Pb}$ are expected to be nearly the same. To estimate the difference we refer to the relative values measured⁵⁵ for the isotopes ^{206}Pb and ^{208}Pb for $E < 15$ MeV. The difference, $\sigma_{208} - \sigma_{206}$, is about 0.2 b for $4 < E < 11$ MeV and about 0.1 b for $11 < E < 15$ MeV. Assuming intermediate values for ^{207}Pb and using the isotopic composition of $^{\text{nat}}\text{Pb}$, we estimate $\sigma_{208} - \sigma_{\text{nat}}$ to be 0.076 b for $4 < E < 11$ MeV and 0.036 b for $11 < E < 15$ MeV. Indeed, if smooth curves were to be drawn through the points of Figs. 7 and 8(a), they would show excellent agreement with these estimated differences.

A smooth visual curve through the Pb points in Fig. 8(a) is a convenient base for comparison of the present ^{208}Pb data with earlier works.^{55,56} For $4 < E < 8$ MeV, the values for σ_{208} from Ref. 55 are about 0.1 b or about 1.5% below such a curve. For $6 < E < 14$ MeV, the σ_{208} values from Ref. 56 are very close to the curve. On the basis of these comparisons and the corresponding comparison above for the present data, we assume the correct curve for $n + ^{208}\text{Pb}$ to be an average of smooth curves through the data from Figs. 7 and 8(a) for $E < 25$ MeV. For $E \geq 25$ MeV we make the approximation $\sigma_{208} = \sigma_{\text{nat}}$. These assumptions are the basis for the cross sections and uncertainties listed in Table I.

Finally, we justify our renormalization of the authors' energies²⁵ for Fig. 8(b). Those data were obtained by time-of-flight techniques using the primitive time-to-height converters available before 1960, whereas the data in Fig. 8(a) were obtained with modern timing methods.

Without the renormalization the two sets of data disagree in energy in the region of overlap, $25 < E < 50$ MeV. Our renormalization by a factor of 1.06 for the energies of the earlier data removes this discrepancy.

There is further evidence of a need for energy renormalization; a factor of 1.04 brings the n-p cross sections for $50 < E < 120$ MeV, also reported in Ref. 25, into agreement with a recent global evaluation⁵⁷ of n-p scattering.

- ¹R. Alarcon, J. Rapaport, and R. W. Finlay, Nucl. Phys. **A462**, 413 (1987).
- ²R. W. Finlay, J. R. M. Annand, T. S. Cheema, J. Rapaport, and F. S. Dietrich, Phys. Rev. C **30**, 796 (1984).
- ³R. W. Finlay, J. R. M. Annand, J. S. Petler, and F. S. Dietrich, Phys. Lett. **155B**, 313 (1985); **157B**, 475 (1985).
- ⁴J. R. M. Annand, R. W. Finlay, and F. S. Dietrich, Nucl. Phys. **A443**, 249 (1985).
- ⁵C. Mahaux and H. Ngô, Nucl. Phys. **A378**, 205 (1982).
- ⁶G. R. Satchler, in *Isospin in Nuclear Physics*, edited by D. H. Wilkinson (North-Holland, Amsterdam, 1969), p. 389.
- ⁷C. B. Dover and Nguyen Van Giai, Nucl. Phys. **A190**, 373 (1972).
- ⁸M. Jaminon and C. Mahaux, Phys. Rev. C **34**, 2097 (1986).
- ⁹C. Mahaux and R. Sartor, Phys. Rev. C **34**, 2119 (1986).
- ¹⁰F. G. Perey and B. Buck, Nucl. Phys. **32**, 353 (1962).
- ¹¹C. Mahaux and H. Ngô, Phys. Lett. **100B**, 285 (1981).
- ¹²Nguyen Van Giai and Pham Van Thieu, Phys. Lett. **126B**, 421 (1983).
- ¹³P. F. Bortignon, R. A. Broglia, C. H. Dasso, and C. Mahaux, Phys. Lett. **140B**, 163 (1984).
- ¹⁴C. Mahaux, P. F. Bortignon, R. A. Broglia, and C. H. Dasso, Phys. Rep. **120**, 1 (1985).
- ¹⁵C. Mahaux, H. Ngô, and G. R. Satchler, Nucl. Phys. **A449**, 354 (1986).
- ¹⁶F. G. Perey, private communication.
- ¹⁷W. R. Smith, Comput. Phys. Commun. **1**, 106 (1969).
- ¹⁸B. Buck, Oxford University report, 1960 (unpublished); G. R. Satchler, private communication.
- ¹⁹D. J. Horen, C. H. Johnson, and A. D. MacKellar, Phys. Lett. **161B**, 217 (1985).
- ²⁰D. J. Horen, C. H. Johnson, J. L. Fowler, A. D. MacKellar, and B. Castel, Phys. Rev. C **34**, 429 (1986).
- ²¹J. Rapaport, T. S. Cheema, D. E. Bainum, R. W. Finlay, and J. D. Carlson, Nucl. Phys. **A296**, 95 (1978).
- ²²R. P. DeVito, Ph.D. dissertation, Michigan State University, 1979 (unpublished); S. M. Austin, private communication.
- ²³C. E. Floyd, Ph.D. dissertation, Duke University, 1981 (unpublished); R. L. Varner, private communication.
- ²⁴J. P. Delaroche, C. E. Floyd, P. P. Guss, R. E. Byrd, K. Murphy, G. Tungate, and R. L. Walter, Phys. Rev. C **28**, 1410 (1983).
- ²⁵P. H. Bowen, J. P. Scanlon, G. H. Stafford, J. J. Thresher, and P. E. Hodgson, Nucl. Phys. **22**, 640 (1961).
- ²⁶R. W. Finlay, private communication.
- ²⁷D. C. Larson, in *Symposium on Neutron Cross Sections from 10 to 50 MeV*, edited by M. R. Bhat and S. Pearlstein, Brookhaven National Laboratory Report BNL-NCS-51245, 1980, p. 277. Data available from the National Nuclear Data Center, Brookhaven National Laboratory.
- ²⁸D. C. Larson, J. A. Harvey, and N. W. Hill (unpublished).
- ²⁹See P. W. Lisowski, G. F. Auchampaugh, M. S. Moore, G. L. Morgan, and R. E. Shamu, in Ref. 27, p. 301.
- ³⁰H. J. Körner and J. P. Schiffer, Phys. Rev. Lett. **27**, 1457 (1971).
- ³¹J. P. Schiffer and H. J. Körner, Phys. Rev. C **8**, 841 (1973).
- ³²M. A. Franey, J. S. Lilley, and W. R. Phillips, Nucl. Phys. **A324**, 193 (1979).
- ³³J. Leigh, T. R. Ophel, D. C. Weisser, and W. R. Phillips, Nucl. Phys. **A382**, 115 (1982).
- ³⁴M. R. Schmorak, Nucl. Data Sheets **22**, 487 (1977).
- ³⁵M. J. Martin, Nucl. Data Sheets **22**, 545 (1977).
- ³⁶S. Galès, Nucleonika **27**, 82 (1982).
- ³⁷S. Galès, G. M. Crawley, D. Weber, and B. Zwieglinski, Phys. Rev. C **18**, 2475 (1978).
- ³⁸J. Guillot, J. Van de Wiele, H. Langevin-Joliot, E. Gerlic, J. P. Didelez, G. Duhamel, G. Perrin, M. Buenerd, and J. Chauvin, Phys. Rev. C **21**, 879 (1980).
- ³⁹J. W. Negele and K. Yazaki, Phys. Rev. Lett. **47**, 71 (1981).
- ⁴⁰C. Mahaux, Phys. Rev. C **28**, 1848 (1983).
- ⁴¹C. Mahaux and H. Ngô, Nucl. Phys. **A431**, 486 (1984).
- ⁴²F. G. Perey, in *Direct Interactions and Nuclear Reaction Mechanisms*, edited by E. Clementel and C. Villi (Gordon and Breach, New York, 1963), p. 125.
- ⁴³J. W. Negele, Phys. Rev. C **9**, 1054 (1974).
- ⁴⁴A. E. L. Dieperink and I. Sick, Phys. Lett. **109B**, 1 (1982).
- ⁴⁵E. N. M. Quint, B. M. Barnett, A. M. van den Berg, J. F. J. van den Brand, H. Clement, R. Ent, B. Frois, D. Goutte, P. Grabmayr, J. W. A. den Herder, E. Jans, G. J. Kramer, J. B. J. M. Lanen, L. Lapikás, H. Nann, G. Van der Steenhoven, G. J. Wagner, and P. K. A. de Witt Huberts, Phys. Rev. Lett. **58**, 1088 (1987).
- ⁴⁶C. N. Papanicolas, L. S. Cardman, J. H. Heisenberg, O. Schwenker, T. E. Milliman, F. W. Hersman, R. S. Hicks, G. A. Peterson, J. S. McCarthy, J. Wise, and B. Frois, Phys. Rev. Lett. **58**, 2296 (1987).
- ⁴⁷C. Mahaux and R. Sartor, Phys. Rev. Lett. **57**, 3015 (1986).
- ⁴⁸C. Mahaux and R. Sartor, Nucl. Phys. **A468**, 193 (1987).
- ⁴⁹J. Rapaport, Phys. Rep. **87**, 25 (1982).
- ⁵⁰A. B. Smith, P. T. Guenther, and R. D. Lawson, Nucl. Phys. **A455**, 344 (1986).
- ⁵¹R. D. Lawson, P. T. Guenther, and A. B. Smith, Phys. Rev. C **34**, 1599 (1986).
- ⁵²A. Lev, W. P. Beres, and M. Divadeenam, Phys. Rev. C **9**, 2416 (1974).
- ⁵³J. Wambach, V. K. Mishra, and Li Chu-Hsia, Nucl. Phys. **A380**, 285 (1982).
- ⁵⁴D. J. Horen, J. A. Harvey, and N. W. Hill, Phys. Rev. C **18**, 722 (1978); **20**, 478 (1979); **24**, 196 (1981).
- ⁵⁵D. G. Foster, Jr. and D. W. Glasgow, Phys. Rev. C **3**, 576 (1971).
- ⁵⁶L. J. Satkowiak, S. M. Ferguson, R. E. Shamu, and M. Soga, Phys. Lett. B **175**, 266 (1986).
- ⁵⁷R. A. Arndt, J. S. Hyslop III, and L. D. Roper, Phys. Rev. D **35**, 128 (1987).